6-2017

Colliding Wind Binaries with Orbital Motion: Line Wind Formulation

Brendan O'Connor
Union College - Schenectady, NY

Colliding Wind Binaries with Orbital Motion: Line Wind Formulation

By

Brendan O'Connor

* * * * * * * * *

Submitted in partial fulfillment

of the requirements for

Honors in the *Department of Physics and Astronomy*

UNION COLLEGE

June, 2017

Abstract

O'CONNOR, BRENDAN Colliding Wind Binaries with Orbital Motion: Line Wind Formulation. Department of Physics and Astronomy, June 2017.
ADVISOR: Francis Wilkin

Stars lose mass in the form of supersonic winds. In a binary star system, these winds collide to produce shockwaves. Such stellar wind collisions are observed in many binary star systems. Due to the orbital motion of the system, a trailing spiral structure is produced. We present a solution method in the co-rotating frame of the stars, which allows us to consider steady state solutions. This requires the inclusion of Coriolis and centrifugal forces, including their effects on the pre-shock winds, for which we were restricted to orbital speed slower than wind speeds. We assume efficient post-shock cooling, which allows us to consider a geometrically thin shell. A set of four ordinary differential equations (ODEs) ensure the conservation of mass and momentum within the shell. It was necessary to develop Taylor series expansions to find self-consistent values that allow for integration of the equations out of the initial singularity. Numerical integration of the equations yields the shell shape. The solution generalizes the analytic solution of Cantó, Raga & Wilkin (1996) to include orbital motion. We further generalize our solution for systems with unequal wind speeds. Systems with unequal wind speeds, but equal wind momentum, produce an asymmetry in the shell that is non-existent for equal wind speeds.

Acknowledgements

The author would like to thank Professor Francis Wilkin of Union College for his incredible support throughout this project, helpful discussions, and patience. This thesis project would not have been possible without his guidance. The author would also like to thank all of the Union College physics and astronomy faculty members for preparing him to undertake this project. The portion of this research carried out in Summer 2016 was possible with support from the Lee L. Davenport Summer Research Fellowship.

Contents

1 Introduction to Colliding Winds

All stars emit winds. A stellar wind is a flow of particles with energies high enough to escape the gravity of the star, and such winds carry matter into space. Stellar winds are mostly made up of a continuous stream of protons, electrons, atoms, ions, molecules, and dust grains depending on the surface temperature of the star. The mass loss rate $\dot{M}$ ranges from $10^{-14} M_{\odot}/\text{yr}$ for the sun through $10^{-8} M_{\odot}/\text{yr}$ for M supergiants to $10^{-4} M_{\odot}/\text{yr}$ for O and B supergiants [2]. The influence of such winds is important in the physics of the interstellar medium (ISM) as a source of chemical enrichment, energy, and momentum. As stated, the mass loss undoubtedly depends on the mass of the star itself. Similarly, the mechanism behind the emission of stellar winds varies based on the mass of the star. In the case of low-mass, cool stars, the wind is caused by the high temperature of the outer layers of the star. For example, in the sun, the solar corona, due to interactions with the sun's magnetic field, is millions of Kelvin. These temperatures give particles in the corona the necessary kinetic energies to escape the gravitation of the sun. In high-mass stars, the winds are driven by radiation pressure from the photons. Opacity in the spectral lines in the outer layers of a high-mass star trap the radiation flux driving a strong wind. The momenta imparted by the escaping photons is large enough to overcome the stellar gravitation and causes surrounding gas to be accelerated away from the star [1]. The wind speed of hot stars is on the order of 3000 km s^{-1} compared to the $400 - 700$ km s^{-1} wind emitted from the sun [1].

In low to intermediate mass stars, while on the main sequence, and on the scale of stellar mass, these mass loss rates are trivial and have no major effect on the star, until possibly when the star reaches the red giant branch and the mass loss increases towards $10^{-6} M_{\odot}/\text{yr}$ [9]. For example, the sun will only have lost about 0.01% of its mass throughout its entire main sequence lifetime [1]. On the red giant branch (RGB), the star's radius becomes increasingly large which causes the surface layers to be only loosely bound by the star's

gravity. Observations show that at the tip of the RGB the mass loss rate of the star increases, earning the name superwind [8]. These superwinds are also observed in asymptotic giant branch stars [3]. Generally, a star of low to intermediate mass will evolve along both the RGB and the AGB before eventually losing an outer envelope of material that expands to form a planetary nebula. In 1975, Dieter Reimers developed a mass-loss scaling law for red giants,

$$\dot{M} = 4 \times 10^{-13}\, \eta\, \frac{LR}{M}\, [M_\odot/\mathrm{yr}] \tag{1.1}$$

with the fitting parameter η given in the range $1/3 < \eta < 3$ and L, R, and M in solar units. The scaling law works well for RGB stars, but is not applicable to those on the AGB [27]. Leitherer et al. also developed models for the output of mass, momentum, and energy from massive stars in the entire upper Hertzsprung-Russell diagram as a function of stellar parameters [30]. The mass loss of red giant stars can also be considered in terms of the Chandrasekhar limit of $1.4M_\odot$ for a star to evolve into a white dwarf. A white dwarf is the final stage of evolution for low-mass main sequence stars, and requires that the star lose enough mass to be below the $1.4M_\odot$ limit [2]. In some cases, the emission of mass throughout the stars lifetime can be enough to create a star of low enough mass.

The case for high-mass stars is different. High-mass main sequence stars lose a significant amount of mass through stellar winds throughout their lifetime [8]. As the star evolves into a supergiant, the mass loss increases drastically [9]. This mass loss can have an effect on their evolution through the Hertzsprung-Russell Diagram, and may cause a different evolutionary sequence depending on the strength of the stellar wind. In some extreme cases, the star sheds completely its outer envelope of hydrogen and is then referred to as a Wolf-Rayet star (WR). In all cases, a star above $8M_\odot$ will end its life in a violent supernova explosion. Supernova explosions are incredibly important factors in local-galactic structure, star formation, and the chemical enrichments of the ISM. Examples of physical parameters for observed stellar binaries are shown in Table 1. These physical systems can

serve as comparison to our models, and are generally useful to develop an understanding of actual binary systems. A subscript 1 indicates the parameters of the primary star, whereas a subscript 2 indicates the secondary.

Parameter (Units)	WR 104	WR 21a	HD 93129A
Period (d)	220 ± 30	31.68 ± 0.013	$> 1.825 \times 10^4$
$\dot{M}_1$ ($M_\odot$ yr$^-$1)	0.8×10^{-5} - 3×10^{-5}	3.16×10^{-5}	10^{-5}
$\dot{M}_2$ ($M_\odot$ yr$^-$1)	6×10^{-8}	2.29×10^{-6}	5.3×10^{-6}
v_{w1} (km s^{-1})	1200	2000	3200
v_{w2} (km s^{-1})	2000	3800	3000

Table 1: Parameters of the systems WR 104 [24], WR 21a [26], and HD 93129A [25].

It is simple to approximate that the speed of stellar winds near the star are on the order of the escape speed. The wind flow begins subsonic and at large distances from the star changes to a supersonic flow when the gravitational attraction from the star is minimal [2]. The wind acceleration is due to gas and radiation pressure. Supersonic stellar wind collisions are a well-studied astrophysical phenomenon. It is observed that the motion of a wind emitting star through space drives the outflowing wind into the interstellar medium developing a bow shock. The name bow shock comes from the wave developed by a ship moving across the ocean. The expelled wind interacts with and sweeps up the surrounding ISM. The bow shock can also be described as the interface between the stellar wind and the ISM, a location at which the flow changes back from supersonic to subsonic and the density changes drastically giving rise to a shock wave. To form a shockwave, the stellar wind must be moving supersonically with respect to the ISM, and the variation in density and pressure between the wind and ISM cannot be small [10]. Mackey et al. notes that a large portion of massive stars are moving supersonically though the ISM [11]. Bow shocks condense the ISM into thin shells that are observed by post-shock emission or scattered light. Many bow shocks, such as the one caused by Betelgeuse, are observed in the mid- and far-infrared [11] due to the scattering of stellar ultraviolet light by dust grains within the shock [12].

Hotter stars may have a spectrum that is dominated by particles within the wind, and not the stellar surface. In this case, emission lines have expansion-type line profiles. Absorption lines have similar profiles with the difference that the profile will be caused strictly by wind material directly in front of the stellar surface [7]. Murdin states that an important aspect of stellar wind observations, in the case of a radiatively driven wind, is line scattering when an electron is either excited or de-excited [1]. This is also, in some cases, the driving factor behind the wind. Winds driven by this process are known as line driven winds. The emitted photon is of an energy near the difference between the two electron energy levels. The detection of this photon corresponds to a range of wavelengths around a line-center. In an accelerating wind, due to radiation from the star, the wavelengths are redshifted due to the Doppler effect which develops a distinctive broad emission line. Line scattering within the wind develops a P-Cygni line profile with a blue absorption dip and red emission peak [1]. P-Cygni profiles are most typically UV resonance transitions to the ground state. The formation of a P-Cygni profile is shown schematically in Figure 1. The blue absorption dip is caused by the scattering of stellar radiation by wind material approaching the observer. On either side of the blue absorption column, both redshifted and blueshifted radiation may be scattered towards the observer which creates a symmetric emission profile around the line center. The combination of the blue-shifted absorption and symmetric emission creates the asymmetric line profile.

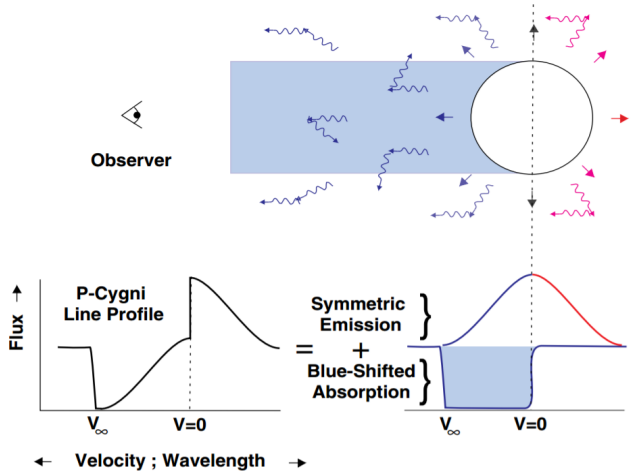

Figure 1: Schematic showing the formation of a P-Cygni line profile. This schematic is borrowed from the Encyclopedia of Astronomy and Astrophysics [1]

In binary star systems, the collision of two radiatively driven winds produces a shocked structure. These systems are called colliding-wind binaries (CWBs) and most generally consist of WR and OB-type stars. When the two winds interact a fraction of the kinetic energy of the winds is converted into heat that causes the shock to emit X-ray, γ-ray, radio or synchrotron radiation [4]. As such, binary systems are commonly observed at these wavelengths. Because of this, the structure and radiation emission of these shocks are worth computing [37][32]. Parkin & Gosset (2011) used a three-dimensional hydrodynamic model to calculate the X-ray emission in the binary system, WR22 [38]. Wilkin et al. (1997) showed that conservation of momentum implies that not all of the kinetic energy may be thermalized, and that the maximum amount available for radiation is the kinetic energy in the center of mass frame [28]. Corcoran explains how in eccentric binaries the X-ray emission can have a high variability based on the density and relative wind velocity along the shock [5]. A common example of a CWB is the system WR-104, which is also observed to have variable X-ray emission. The system consists of a WR star and a brighter OB main sequence star, and the shocked structure has an observed Archimedian spiral shape due to the orbital motion of the system [13]. X-ray emission is also observed in the Eta Carinae binary star system. Johnstone et al. modeled the low-mass counterpart

to CWBs to determine the habitability of planets in surrounding regions to the shock [6]. Hydrodynamical simulations have been successful in determining the shape of these structures in two- and three-dimensions, [29][24][31] but simple analytic models have yet to be found when both Coriolis and centrifugal forces are accounted for.

Thin shell analytic models have been constructed for simplified geometries [33][34][35]. The collision surface is a shell of fluid bounded by two shock surfaces resulting from the deceleration of the winds. If it is assumed that within the shock there is efficient cooling, then it is implied that the shocked layers of fluid have small thickness when compared to their distance from the star [15]. Using this assumption, Wilkin (1996, hereafter W96) developed exact analytic solutions for stellar wind bow shocks using momentum conservation arguments [15]. Cantó, Raga, & Wilkin (1996, subsequently CRW96) built on the formalism of W96, and applied similar methods to the interaction of two supersonic, stellar winds [16]. These models are applicable in an inertial frame and ignore the orbital motion of the binary system. This paper builds on these theoretical models, and examines the problem of an orbiting binary star system with supersonic wind collision. This requires conservation of mass and momentum arguments to derive and solve four ordinary differential equations to determine the shape of the collision surface for winds with equal momentum loss rates.

1.1 Introducing the Line Wind

We introduce the concept of a line wind to make the geometry of the system more tractable. As its name suggests, a line wind emits fluid radially from a line and exhibits both cylindrical and plane symmetry. There is a precedent for considering cylindrical winds, such as 2D simulations [24][36]. Lamberts et al. (2012) state that performing 2D simulations in the orbital plane of the star involves a density that scales as r^{-1} instead of r^{-2} as it would for an isotropic wind [24]. The mass-loss rate per unit length of a line wind is defined as $\lambda \equiv \mathcal{F}\ A/2\pi L$ where $\mathcal{F}$ is the mass flux and A is the area of a cylindrical

Gaussian surface enclosing the line (ignoring the caps, since all wind is emitted radially). The density of the wind can be written as,

$$\rho = \frac{\lambda}{rv}, \tag{1.2}$$

where v is the launch speed of the wind and r is the cylindrical radius measured from the line wind. Due to the plane symmetry of a line wind, we need only determine the wind properties for a slice of arbitrary thickness in the orbital plane. This removes one independent and one dependent variable. We further assume the speed v is constant in an inertial frame so that it is a coasting wind.

The line wind formulation, as a result of the simplified geometry, will serve as a stepping stone for further progress in this field, and will be used to develop the necessary tools to solve the more difficult problem of an isotropic wind collision. In this paper, we first derive the results of CRW96 with the simplification of the line wind geometry in Section 1.2. Second, in Section 2, we apply the formalism of W96, CRW96, and Wilkin & Stahler (1998, hereafter WS98) to the interaction of two, constant velocity solar winds in the steady state limit accounting for orbital motion. In Section 3, we determine the shell shape in the unequal wind case, where one wind has a higher velocity or mass-loss rate than the other wind.

1.2 Stationary Line Wind Collisions

In this section, we consider the momentum and mass conservation arguments of CRW96, simplifying the two-wind interaction problem with the line wind geometry. The steady-state collision of two nonaccelerated line winds in the yz-plane develops a thin shocked shell, where we choose these coordinates to agree with the solutions of CRW96. Due to the cylindrical symmetry of the line winds, we need only consider the yz-plane, with the line

winds parallel to the x-axis. The first line wind is located at the origin while the second line wind is at $z = D$. The curve of the thin shell can be specified as $R(\theta_1)$, where R is the spherical radius. The winds collide head-on at a radius, referred to as the stagnation point, determined by balancing the ram pressures of the winds, $\rho_1 v_1^2 = \rho_2 v_2^2$, which provides,

$$R_o = \frac{\lambda_1 v_1}{\rho_2 v_2^2}, \tag{1.3}$$

where the wind at the origin is denoted by subscript 1 and the second wind is denoted by subscript 2. Note that for equal winds the stagnation point is equidistant between the two winds at $R_o = D/2$. The stagnation point radius, R_o, serves as the unit of length, and scales the shape of the shell in non-dimensional form. A schematic of this situation is shown in Figure 2.

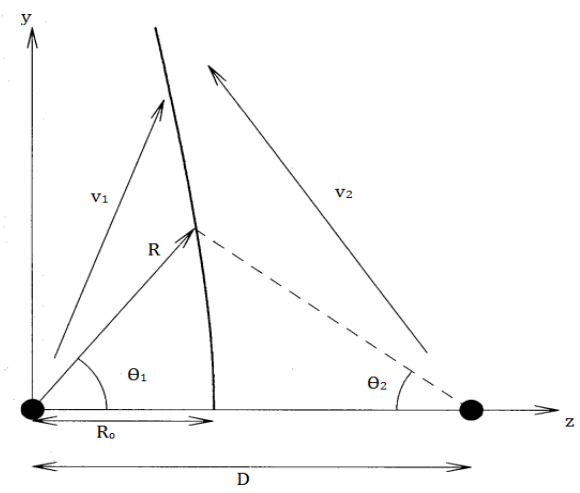

Figure 2: Schematic diagram of the line wind collision. The two winds are shown by the filled black circles: the first wind is at the origin, and the second wind is at a distance D along the z-axis. The thin shell, given by $R(\theta_1)$, is represented and clearly intercepts the z-axis at the stagnation point R_o. This figure has been borrowed from CRW96, where we have changed the labels to match the geometry of this problem [16].

1.2.1 Flux Function Description of Momentum Conservation

The condition of steady state requires that the flow rates of mass and momentum within the shell are equal to the mass and momentum incident upon the shell from both winds integrated from the stagnation point to θ_1 [16]. It is important to develop an understanding of flux functions, as they will be an important aspect of this section and later sections. A flux is defined as the rate of flow of a property per unit area. By this definition, Φ_m, is the mass flow rate through a disk of the shell with height Δx at an angle θ_1 from the stagnation point and is given by [15],

$$\Phi_m = \sigma v_t, \tag{1.4}$$

which can be used to solve for the mass surface density σ and tangential velocity v_t within the shell. Due to the fact that the flow rate of mass in the shell is equal to the mass striking the shell from both winds, $\Phi_m = \Phi_{m1} + \Phi_{m2}$. We use a subscript 1 to represent the first wind, and a 2 to indicate the second wind. The velocity may be written in terms of flux functions as $\vec{v} = \vec{\Phi}/\Phi_m$ with $\vec{\Phi}$ representing the linear momentum flux. This momentum flux and velocity is in fact tangent to the shell so by dotting by the unit vector $\hat{t}$ we find $v_t = \Phi_t/\Phi_m$ where Φ_t is the momentum flux tangential to the shell given by $\sqrt{\Phi_y^2 + \Phi_z^2} = \Phi_m v_t$. The same definition used for Φ_m readily applies to momentum fluxes where instead of mass the momentum flow rate is considered. Therefore, the quantities Φ_y and Φ_z are the momentum rates in the y and z directions through a disk of the shell with height Δx at an angle θ_1 from the stagnation point. Returning to the condition of steady state, the conservation of mass and momentum within the shell gives the linear momentum flux,

$$\Phi_y \hat{y} + \Phi_z \hat{z} = [\Phi_{y1} + \Phi_{y2}]\hat{y} + [\Phi_{z1} + \Phi_{z2}]\hat{z}, \tag{1.5}$$

which can be related to the mass flux by,

$$\Phi_y \hat{y} + \Phi_z \hat{z} = \Phi_m [v_y \hat{y} + v_z \hat{z}]. \tag{1.6}$$

The angular momentum flux Φ_j is defined by,

$$\vec{\Phi}_j = \vec{R} \times \vec{\Phi}. \tag{1.7}$$

If we define the θ-component of velocity within the shell as $v_\theta = v_y \cos\theta_1 - \mathrm{v_z} \sin\theta_1$, where the angle θ_1 is shown in Figure 2. Then the angular momentum flux is related to the components of linear momentum flux as,

$$\vec{\Phi}_j = \Phi_m v_\theta R\, \hat{\phi}, \tag{1.8a}$$

$$\vec{\Phi}_j = R(\Phi_y \cos\theta_1 - \Phi_z \sin\theta_1)\hat{\phi}, \tag{1.8b}$$

because the angular momentum is only in the $\hat{\phi}$-direction we will only use the ϕ-component of angular momentum flux $\Phi_j = \vec{\Phi}_j \cdot \hat{\phi}$. Conservation of angular momentum implies,

$$\Phi_j = \Phi_{j1} + \Phi_{j2}. \tag{1.9}$$

Using Equations 1.5, 1.6, 1.8, and 1.9 we find the curve of the shell in algebraic form to be,

$$R = \frac{\Phi_{j1} + \Phi_{j2}}{(\Phi_{y1} + \Phi_{y2})\cos\theta_1 - (\Phi_{z1} + \Phi_{z2})\sin\theta_1}, \tag{1.10}$$

where the quantities on the right side of the equation are functions of θ_1, θ_2, and R, and therefore describe the spherical radius at any position along the shell. Equation 1.10 has the same form as Equation 6 of CRW96 although the definitions of the flux functions have been altered due to the line wind geometry.

1.2.2 Formulation and Solution of the Flux Functions

In this section, we use the schematic shown in Figure 2 to derive the mass and momentum imparted on the shell by both winds. The flux function definitions given in the last

section are seen clearly here. For example, consider the mass flux on the shell by the first wind,

$$\Phi_{m1} = \int_0^{\theta_1} d\Phi_{m1} = \int_0^{\theta_1} \lambda_1 d\theta_1 = \lambda_1 \theta_1. \tag{1.11}$$

It seen that the mass flux is the mass sent into the shell by the first wind integrated from the direction of the symmetry axis to the angle θ_1. This comes directly from the definition of Φ_m. Following this integration method for the rest of the flux components, we find the linear and angular momentum propelled into the shell by the first wind to be,

$$\Phi_{z1} = \int_0^{\theta_1} v_1 \cos\ \theta_1\ d\Phi_{m1} = \lambda_1 v_1 \sin\theta_1, \tag{1.12a}$$

$$\Phi_{y1} = \int_0^{\theta_1} v_1 \sin\ \theta_1\ d\Phi_{m1} = \lambda_1 v_1 (1 - \cos\theta_1), \tag{1.12b}$$

$$\Phi_{j1} = 0, \tag{1.12c}$$

and similar equations are written for the second wind,

$$\Phi_{m2} = \int_0^{\theta_2} d\Phi_{m2} = \int_0^{\theta_2} \lambda_2 d\theta_2 = \lambda_2 \theta_2, \tag{1.13a}$$

$$\Phi_{z2} = \int_0^{\theta_2} -v_2 \cos\ \theta_2\ d\Phi_{m2} = -\lambda_2 v_2 \sin\theta_2, \tag{1.13b}$$

$$\Phi_{y2} = \int_0^{\theta_2} v_2 \sin\ \theta_2\ d\Phi_{m2} = \lambda_2 v_2 (1 - \cos\theta_2), \tag{1.13c}$$

$$\Phi_{j2} = \int_0^{y} D v_2 \sin\ \theta\ d\Phi_{m2} = D\lambda_2 v_2 (1 - \cos\theta_2). \tag{1.13d}$$

We define a dimensionless parameter β representing the momentum ratio of the line winds,

$$\beta = \frac{\lambda_1 v_1}{\lambda_2 v_2}. \tag{1.14}$$

The case of equal momentum loss rates is $\beta = 1$. Lamberts et al. (2011) gives the stagnation point radius in terms of β in their treatment of 2D cylindrical winds,[36]

$$R_o = \frac{1}{1+\beta^{-1}} D. \tag{1.15}$$

Lamberts et al. (2011) similarly applied the CRW96 formalism to cylindrical winds in order to determine a 2D solution comparable to CRW96 Equation 24. We continue our treatment of the problem by replacing Equations 1.11, 1.12 and 1.13 in Equation 1.10 and through use of the geometric relation determined from the sine law,

$$R = D \sin\theta_2 \csc(\theta_1 + \theta_2), \tag{1.16}$$

we obtain,

$$\tan\left(\frac{\theta_1}{2}\right) = \beta \tan\left(\frac{\theta_2}{2}\right). \tag{1.17}$$

For $\beta = 1$, it is clear from Equation 1.17 that $\theta_1 = \theta_2$. For arbitrary values of β and a given value of θ_1, Equation 1.17 can be solved for θ_2 using the relation,

$$\theta_2 = 2\tan^{-1}\left(\frac{1}{\beta}\tan\left(\frac{\theta_1}{2}\right)\right), \tag{1.18}$$

and the spherical radius of the shell can be determined by Equation 1.16. Our analytic solution for θ_2 is an explicit solution, whereas Lamberts et al. (2011), like CRW96, gives an implicit solution. Either solution, when compared to CRW96 Equation 24, demonstrates the simplified nature of the line wind geometry.CRW96 required numerical solution methods to find the value of θ_2 whereas the line wind solutions are analytic. As done by CRW96, an approximate solution can be found for θ_2 using,

$$\theta_2 \approx \frac{1}{\beta}\theta_1 + \frac{\beta^2-1}{12\,\beta^3}\theta_1^3 + \frac{2\beta^4-5\beta^2+3}{240\,\beta^5}\theta_1^5, \tag{1.19}$$

which comes from the expansion of Equation 1.18 for small θ_1, as we expect θ_1 to be small for low values of β.

The combination of Equations 1.18 and 1.16 produce the shape of the shell. For equal strength winds, we observe a constant plane at $z = D/2$ as shown in Figure 3.

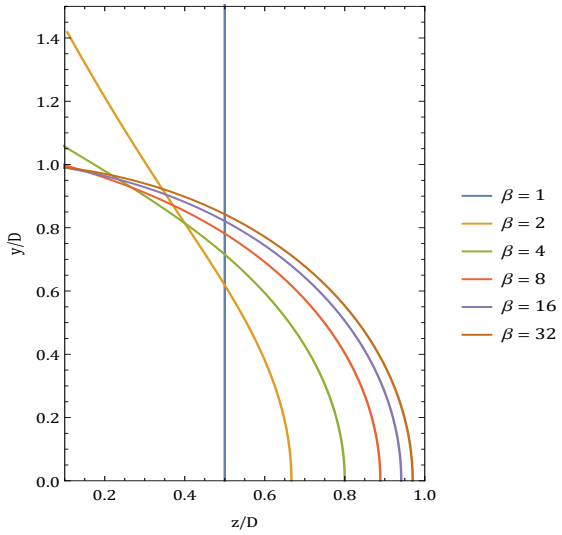

Figure 3: The locus of the thin shell for different values of the parameter β.

In Figure 3, the curve for $\beta = 1$ is the collision surface for a system with no orbital motion in the case of equal winds. This is an important check to ensure that the solutions in Section 2 for the corotating line wind problem are correct for the most basic situation. It is also worth noting that W96's bow shock solution can be simplified by the concept of a line wind [15].

The asymptotic angle $\theta_{\infty 1}$, corresponding to $R \to \infty$, can be found by evaluating Equation 1.17 for the condition $\theta_{\infty 1} + \theta_{\infty 2} = \pi$,

$$\theta_{\infty 1} = \pi - 2 \tan^{-1} \sqrt{\beta}. \tag{1.20}$$

$\theta_{\infty 1}$ represents the tail solution for the bow shock at distance much greater than the stellar separation distance. We plot Equation 1.20 in Figure 4 as a function of β. It is clear that for

$\beta = 0$, $\theta_{\infty 1} = 180°$ which indicates that at large distances from the origin the bow shock is parallel to the z-axis.

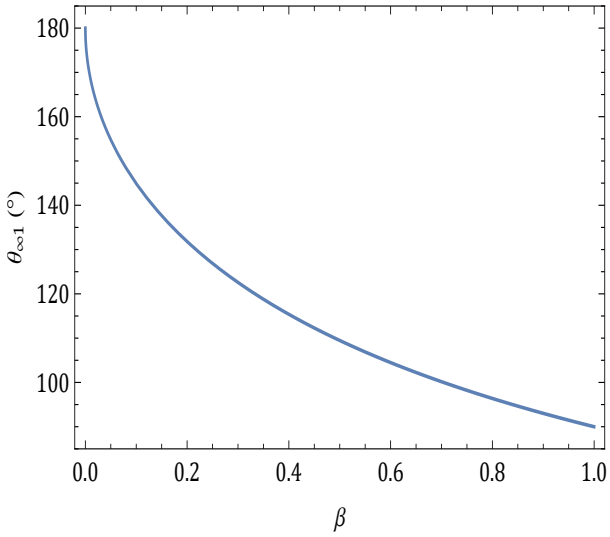

Figure 4: The asymptotic angle $\theta_{\infty 1}$ is shown as a function of β.

1.2.3 Mass Surface Density and Tangential Velocity

We find the tangential velocity through the use of Equations 1.5 and 1.6,

$$v_t = \frac{\sqrt{\Phi_y^2 + \Phi_z^2}}{\Phi_m}. \tag{1.21}$$

Inserting the necessary information from Equations 1.12 and 1.13,

$$\frac{v_t}{v_{w1}} = \frac{\sqrt{[\beta(1 - \cos\ \theta_1) + (1 - \cos\ \theta_2)]^2 + [\beta\ \sin\ \theta_1 - \sin\ \theta_2]^2}}{\beta\ \theta_1 + \alpha\ \theta_2}, \tag{1.22}$$

where $\alpha = v_{w1}/v_{w2}$. As stated above, the mass surface density can be found using Equation 1.4,

$$\sigma = \frac{\Phi_m^2}{\Phi_t}. \tag{1.23}$$

Using Equations 1.12 and 1.13, we find σ to be,

$$\sigma = \frac{\sigma_o \, (\beta \, \theta_1 + \alpha \, \theta_2)^2}{\sqrt{[\beta(1 - \cos \, \theta_1) + (1 - \cos \, \theta_2)]^2 + [\beta \, \sin \, \theta_1 - \sin \, \theta_2]^2}}, \tag{1.24}$$

and $\sigma_o = \lambda / \beta v_{w1}$. The tangential velocity and mass surface density are plotted in **Figures 5a** and **5b** for multiple values of β.

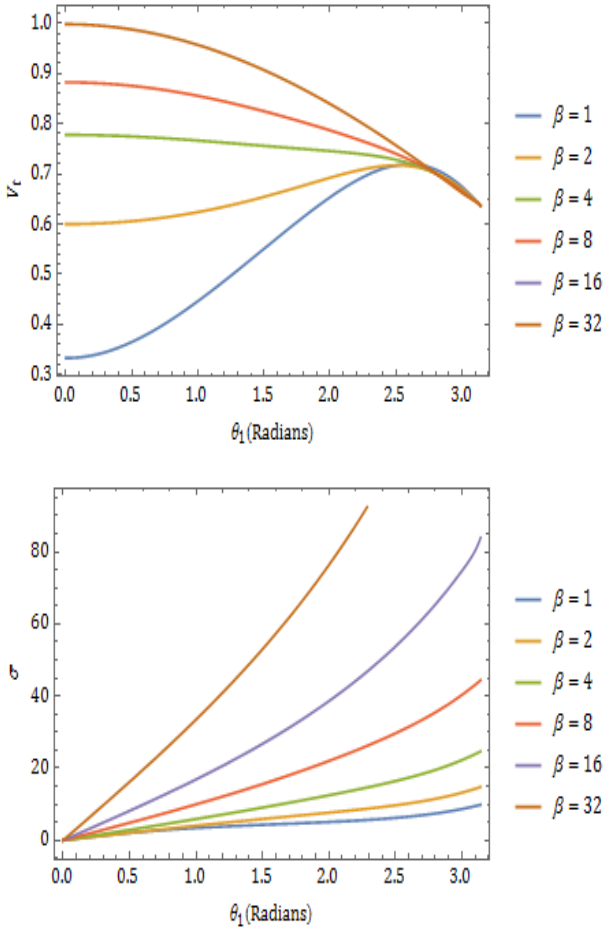

Figure 5: The tangential velocity (left) and mass surface density (right) for several β values ranging from 1 to 32.

For the case of equal winds, $\beta = 1$, it is clear from Equation 1.17 that $\theta_1 = \theta_2$. In this

special case, Equations 1.22 and 1.24 can be rewritten in a simpler form,

$$\frac{v_t}{v_{w1}} = 2\frac{(\cos\ \theta_1 - 1)}{\theta_1(1+\alpha)}, \tag{1.25a}$$

$$\sigma = \sigma_o \frac{\theta_1^2(1+\alpha)^2}{2(1-\cos\ \theta_1)}. \tag{1.25b}$$

Equation 1.16 can likewise be written in simpler form,

$$R = \frac{D}{2}\ \sec\ \theta_1. \tag{1.26}$$

CRW96 notes that it is possible to carry out a series solution to find approximate, explicit solutions to the two-wind interaction problem. We follow this suggestion and produce series solutions for R, v_t and σ. When β is left as an arbitrary value, Equations 1.16, 1.22, and 1.24 can be Taylor expanded in orders of θ_1. This is done by first inserting Equation 1.18 into Equations 1.16, 1.22, and 1.24. The first two non-zero terms of the Taylor expansions are,

$$\frac{R}{D} = \frac{1}{1+\beta} + \frac{1}{4\,\beta}\,\theta_1^2 + \frac{\beta(3+2\beta)}{48\,\beta^2}\,\theta_1^4, \tag{1.27a}$$

$$\frac{v_t}{v_{w1}} = \frac{\beta\sqrt{\beta^2+\frac{1}{\beta^2}-2}}{\alpha+\beta^2} + \frac{-\alpha+(2\alpha-3)\beta^2+6\alpha\beta^3+8(1+\alpha)\beta^4+6\beta^5+(2-3\alpha)\beta^6-\beta^8}{24\,\beta^3\,(\alpha+\beta^2)^2\sqrt{\beta^2+\frac{1}{\beta^2}-2}}\,\theta_1^2, \tag{1.27b}$$

$$\frac{\sigma}{\sigma_o} = \frac{(\alpha+\beta^2)}{\beta^2\sqrt{\beta^2+\frac{1}{\beta^2}-2}}\,\theta_1 - \frac{(\alpha+\beta^2)(\beta^2(3+\beta(\beta(-1+\beta)^2-6)+\alpha(\beta(2+\beta(1+5(-2+\beta)\beta))-1}{24(\beta^2-1)^2\beta^4\sqrt{\beta^2+\frac{1}{\beta^2}-2}} \tag{1.27c}$$

1.3 Importance of Orbital Motion in Binary Wind Collisions

Binary star systems are relevant in astrophysics due to the fact that two-thirds of all stars in the Milky Way are in binaries [2]. In a binary system, both stars emit winds, which collide supersonically to produce a shocked structure. In this section, we describe the necessity of including orbital motion when modeling such shocks.

We consider the problem of two line winds orbiting a common center of mass. In the co-rotating frame, due to orbital motion, the winds are anisotropic resulting in a nonaxisymmetric shock geometry. The winds collide with balanced ram pressures at the midpoint between the stars, which for equal winds is referred to as the stagnation point. Due to the symmetry of the co-rotating frame, we develop this solution method under the assumption of steady state. For steady state collisions, gas strikes the shell from both sides and cannot accumulate at any given location. Instead, a flow of gas emanates from the region surrounding the stagnation point.

The orbital motion of the system adds complexity and breaks the symmetry implied in the hypothetical, unmoving binary wind solution in Section 1.2. To describe the bow shock in a co-rotating reference frame we must account for the effects of the Coriolis and centrifugal forces. These forces act on the shock structure to develop a spiral pattern, as seen in direct observations of binary systems in Figure 6. We develop additional methods for integrating the Coriolis and centrifugal forces into the solution method described by W96, CRW96, and WS98.

In Section 2, we formulate the problem of wind collisions in a rotating binary system by first presenting the streamline descriptions of WH17. Followed by an explanation of conservation of mass and momentum arguments to develop and solve four ordinary differential equations for the shape of the collision surface in the case of equal winds. In Section 3, we apply a similar formalism to the case of unequal winds. We conclude in Section 4

with a summary of the important results and possible future research in this field.

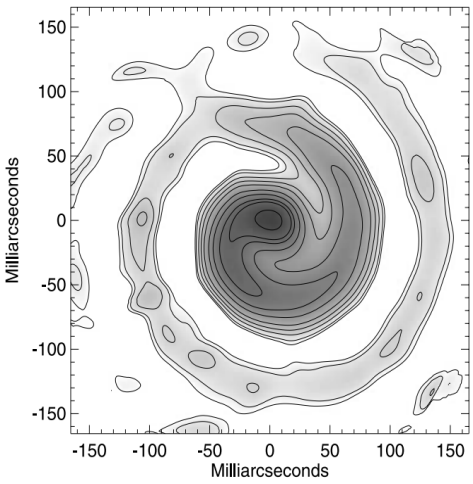

Figure 6: Image of the binary system, WR104, showing the spiral pattern of the shock induced by orbital motion [14].

2 Mathematical Formulation: Equal Winds

In this section, we present an extension to the formalism described in Section 1.2 to the problem of a binary line wind system with orbital motion. The solution requires a description of stellar wind streamlines (Appendix A) in the co-rotating frame which were found by Wilkin & Hausner (2017), hereafter WH17. In this section, we assume that the line winds have equal mass-loss rates and equal wind speeds. The two supersonic line wind flows collide at the origin in the co-rotating frame to form a thin shell in the steady state limit.

2.1 Description of an Orbiting Line Wind

We consider a binary line wind system in a counter-clockwise, circular orbit as viewed from above. The system has plane symmetry, and therefore we need only apply this formalism to the orbital plane. In the reference frame of the line winds, there is a steady-state solution for the trajectory and velocity of the emitted winds.

The line wind orbits at a distance R_o from the origin in the xy-plane with an angular frequency ω. The star's position and velocity in the inertial frame are described by,

$$\vec{r}_*(t) = R_o(\hat{x}\cos\omega\mathrm{t} + \hat{\mathrm{y}}\sin\omega\mathrm{t}), \tag{2.1a}$$

$$\vec{v}_*(t) = \omega R_o(-\hat{x}\sin\omega\mathrm{t} + \hat{\mathrm{y}}\cos\omega\mathrm{t}), \tag{2.1b}$$

where $\hat{x}$ and $\hat{y}$ represent unit vectors parallel to the familiar x and y axes. The trajectory of a fluid element launched at time τ in the inertial frame is given by,

$$\vec{R}(\tau) = \vec{r}_*(t) + (t-\tau)[\vec{v}_*(t) + \vec{v}'_w(\theta, s)] \tag{2.2}$$

where $\vec{v}'_w(\theta, s)$ is the launch velocity in the reference frame of the line wind and $t > \tau$. The

prime denotes the corotating frame. The launch velocity in the corotating frame is,

$$\vec{v}'_w(\theta, s) = -\hat{x}\cos(\theta - \omega\tau) - \hat{y}\sin(\theta - \omega\tau). \tag{2.3}$$

The equations relating the inertial and co-rotating coordinate systems are,

$$x = x' \cos \omega \mathrm{t} - \mathrm{y}' \sin \omega \mathrm{t}, \tag{2.4a}$$

$$y = -x' \sin \omega \mathrm{t} + \mathrm{y}' \cos \omega \mathrm{t}, \tag{2.4b}$$

where we have chosen not to consider the z axis due to the cylindrical symmetry of the line wind, and x' and y' represent the coordinates of the co-rotating frame as seen in Figure 7.

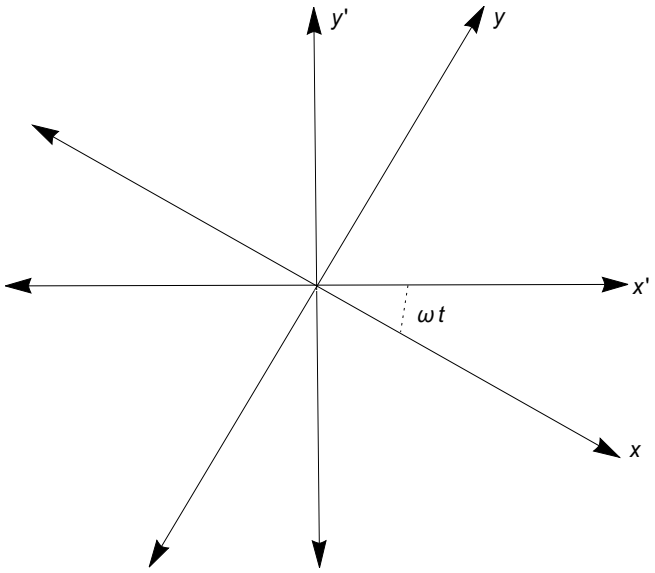

Figure 7: The Cartesian coordinates in the inertial and co-rotating reference frames. Primes denote the co-rotating coordinates.

2.1.1 Fluid Trajectory and Velocity

The path of a fluid element launched at time τ from the star's location is described by WH17 [18]. The equations of WH17 take forms suitable for a line wind when the azimuthal angle $\alpha = \theta + \pi$ and the latitude $\delta = 0$. Because line winds are 2D, we can safely set

the latitudinal angle to zero. Note, the α used by WH17 is not the ratio of wind speeds that we use for the remainder of this work, but instead is a longitudinal angle measured counterclockwise from the x'-axis. As defined in WH17, the dimensionless trajectory, in the co-rotating frame, of a fluid element launched from a line wind at $\vec{r}'_* = (R_o, 0)$ is,

$$\begin{aligned}\vec{r}' =&\langle \cos(ps) + ps\ \sin(ps) - s\ \cos(\theta - ps), \\ &-\sin(ps) + ps\ \cos(ps) - s\ \sin(\theta - ps)\rangle,\end{aligned} \tag{2.5}$$

where p and s are dimensionless parameters, and θ represents the azimuthal launch angle of a streamline measured counter clockwise relative to the $-x'$-axis. The dimensionless parameter s represents the time since launch, $(t - \tau)R_o/V_w$, of a specific streamline to a point on the streamline. The dimensionless constant p designates the ratio of the orbital speed of the star to the launch speed of a fluid element from the star, $p = \omega R_o/V_w$. The combination of these two dimensionless parameters, ps, represents the angle in radians that the line wind has rotated along its orbit since the launch of a fluid element.

The dimensionless velocity of a fluid element can be found by differentiating Equation 2.5 with respect to s, which produces the components,

$$u'_x = -\cos(\theta - ps) - ps\ \sin(\theta - ps) + p^2 s\ \cos(ps), \tag{2.6a}$$

$$u'_y = -\sin(\theta - ps) + ps\ \cos(\theta - ps) - p^2 s\ \sin(ps). \tag{2.6b}$$

Equations 2.5 and 2.6 are the complete streamline descriptions provided by WH17. We can compare these results to a system with no orbital motion by taking the limit that $p \to 0$.

2.1.2 Fluid Density

We follow the method outline by WH17 to find the fluid density, ρ, as a function of position. It is not as simple as the trajectory and velocity where we set the latitude $\delta = 0$,

we re-derive the fluid density from scratch using the steps of WH17. This is done by solving the mass conservation equation. First, we recall the density of a line wind used in Section 1.2 which is given by Equation 1.2. Similarly, we define the unit of density as,

$$\rho_o = \frac{\lambda}{r_* u_w}, \tag{2.7}$$

where r_* is the unit of length and u_w is the unit of velocity. The dimensionless density is therefore $\tilde{\rho} = \rho/\rho_o$. The mass conservation equation is,

$$\nabla \cdot (\tilde{\rho}\vec{u}') = 0, \tag{2.8}$$

where $\vec{u}'$ is the vector sum of Equation 2.6. WH17 used tensor calculus to solve for the density, we follow a similar approach recognizing that our set of coordinates is $(z^i) = (\theta, s)$ due to that fact that $\delta = 0$ for a line wind. The superscript, in this case, is an index which is either θ or s. The covariant basis vectors are found by,

$$\mathbf{b}_i = \frac{\partial \vec{r}'}{\partial z^i}, \tag{2.9}$$

with $\vec{r}'$ equivalent to Equation 2.5. The basis vectors are,

$$\mathbf{b}_\theta = \hat{x}' s \sin(\theta - ps) - \hat{y}' s \cos(\theta - ps), \tag{2.10}$$

and $\mathbf{b}_s = \vec{u}'$. The magnitude square of the basis vectors are,

$$u'^2 = 1 + p^2 s[s(1 + p^2) - 2(\cos\theta + ps\sin(ps)], \tag{2.11a}$$

$$|\mathbf{b}_\theta|^2 = s^2. \tag{2.11b}$$

It naturally follows that the covariant metric tensor is simpler for a line wind and is,

$$\mathbf{g} = \begin{pmatrix} s^2 & \mathrm{g}_{\theta s} \\ \mathrm{g}_{s\theta} & u'^2 \end{pmatrix} \tag{2.12}$$

where $\mathrm{g}_{\theta s} = \mathrm{g}_{s\theta} = \mathbf{b}_\theta \cdot \mathbf{b}_s = ps^2(p\sin\theta - 1)$.The determinant, g, of the metric tensor is,

$$\mathrm{g} = s^2(1 - p^2 s\cos\theta)^2. \tag{2.13}$$

This yields the density law of a similar form to WH17,

$$\nabla \cdot \mathbf{A} = \frac{1}{\sqrt{\mathrm{g}}}\Big[\frac{\partial}{\partial\theta}(\sqrt{\mathrm{g}}\mathrm{A}^\theta) + \frac{\partial}{\partial s}(\sqrt{\mathrm{g}}\mathrm{A}^s)\Big]. \tag{2.14}$$

Following WH17, we note that only the second term of the divergence is required, as the first term vanishes when applying the above formula to Equation 2.8. To do this, we apply $\mathbf{A} = \tilde{\rho}\vec{u}'$, recognizing that the only non-vanishing curvilinear component is the s component because $u'_\theta = 0$ and $u'_s = 1$. Therefore, the solution is,

$$\sqrt{\mathrm{g}}\,\tilde{\rho} = f(\theta). \tag{2.15}$$

The function $f(\theta)$ is found by matching the behavior of Equation 2.15 near the line wind where the flow is cylindrically-symmetric in the limit of small s. Taking the limit as $s \to 0$, $\sqrt{\mathrm{g}}$ drops its dependence on θ. This requires that $f(\theta)$ is a constant. If we regard the mass density at a small radius $R_1 = R_o s_1$ measured from the source we find,

$$\rho_1 = \frac{\lambda}{R_1 u_w} = \rho_o \frac{f(\theta)}{\sqrt{\mathrm{g}}}, \tag{2.16}$$

which gives us,

$$\rho = \frac{\lambda}{R_o u_w}\frac{1}{s(1 - p^2 s\cos\theta)}. \tag{2.17}$$

In dimensionless form this is written as,

$$\tilde{\rho} = \frac{1}{s(1 - p^2 s\cos\theta)}. \tag{2.18}$$

There is a density enhancement for inner streamlines, and notably less dense outer streamlines for $\theta > \pi/2$.

2.1.3 Description of the Second Wind

WH17 provided the trajectory and velocity of a fluid element launched from a line wind at $\vec{r}' = (R_o, 0)$, but we also require a wind description for the second line wind at $\vec{r}_2' = (-R_o, 0)$. The wind descriptions for the second line wind develop from the inherent skew symmetry of the co-rotating frame in a binary system. Consider a point (x_o, y_o) on the shell closer to the first wind, which we will refer to as point A. There is a skew symmetric point $(-x_o, -y_o)$ referred to as point B. By symmetry, the wind description of the first wind at point B is equivalent to the wind description of the second wind at point A. We find that $\vec{r}_2'(\theta_2, s_2) = -\vec{r}_1'(\theta_1, s_1)$ which in turn yields the result $\vec{u}_2'(\theta_2, s_2) = -\vec{u}_1'(\theta_1, s_1)$. Figure 8 is a depiction of the diagram used to determine this geometry.

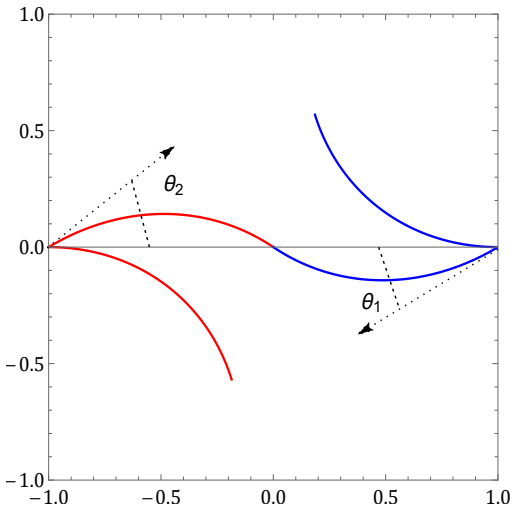

Figure 8: Diagram depicting the evident skew symmetric nature of streamlines in the co-rotating frame. The launch angles θ_1 and θ_2 are measured from their respective source.

We rewrite Equation 2.2 for the second line wind as,

$$\vec{R}_2(\tau) = -\vec{R}(\tau)$$
$$\vec{R}_2(\tau) = -\vec{r}_*(t) - (t-\tau)[\vec{v}_*(t) + \vec{v}'_w(\theta, s)], \tag{2.19}$$

the subscript 2 denotes the second wind, and the equations in Section 2.1.1 take on subscript 1 to represent the first line wind. The nondimensional description of streamlines from the second line wind return,

$$\vec{r}'_2 = \langle -\cos(ps_2) - ps_2\ \sin(ps_2) + s_2\ \cos(\theta_2 - ps_2), \tag{2.20a}$$
$$\sin(ps_2) - ps_2\ \cos(ps_2) + s_2\ \sin(\theta_2 - ps_2)\rangle,$$
$$u'_{2x} = \cos(\theta_2 - ps_2) + ps_2\ \sin(\theta_2 - ps_2) - p^2 s_2\ \cos(ps_2), \tag{2.20b}$$
$$u'_{2y} = \sin(\theta_2 - ps_2) - ps_2\ \cos(\theta_2 - ps_2) + p^2 s_2\ \sin(ps_2), \tag{2.20c}$$

where $\vec{r}'_2$, u'_{2x}, and u'_{2y} are the dimensionless trajectory and velocity components of a fluid element. Similar to the descriptions of the first wind, θ_2 and s_2 represent the coordinates of a fluid element along a streamline measured from the location of the second wind. The wind launch angle, θ_2, is an azimuthal angle measured counter-clockwise from the top of the x-axis as seen in Figure 8. For equal winds, the fluid density, Equation 2.18, remains the same for both winds.

The streamline trajectories for both winds are shown in Figure 9 for $p = 0.6$. It is clear from the figure that the streamlines are not radial as s increases, though they are emitted radially, due to the Coriolis and centrifugal forces in the co-rotating frame. In the inertial frame, fluid emitted from the winds moves radially.

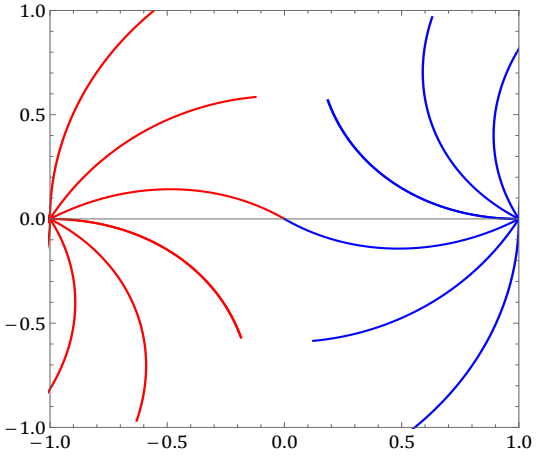

Figure 9: Stellar wind streamlines in the orbital plane from winds at $x/R_o = -1$ and $x/R_o = 1$ for $p = 0.6$.

2.1.4 Derivation of the Critical Streamlines

There exists a specific value of θ and s for each wind that signifies a streamline through the origin, as shown in Figure 9. The origin is the location of the stagnation point, and as such the streamlines that strike the origin collide anti-parallel and have balancing ram pressures. We define θ_o and s_o as the critical streamline labels that represent the critical streamline through the origin.

As noted above, fluid elements in the inertial frame move in a straight path. For a streamline to reach the origin in the inertial frame we require that $\hat{v}_w = -\hat{r}$, which states that the velocity of a fluid element emitted from the line wind must be anti-parallel to the stars position vector from the origin, given by Equation 2.1a. $\vec{v}_w$ is the orbital velocity of the line wind given by Equation 2.1b plus the velocity of the wind emitted from the source in the co-rotating frame. Using the relation $\vec{v}_w \cdot \hat{r} = -|\vec{v}_w|$, and assuming $t = \tau = 0$ with no loss of generality, we find,

$$\theta_o = \arcsin\ p. \tag{2.21}$$

To solve for s_o we use the relation,

$$x = x_o + u_x T, \tag{2.22}$$

plugging in the values for x and x_o,

$$0 = R_o + u_x T, \tag{2.23}$$

where $T = R_o/v_w$ is the unit of time. Through the use of this equation, and by utilizing the trigonometric identity developed by Equation 2.21,

$$\cos\ \theta = \sqrt{1 - p^2}, \tag{2.24}$$

we determine,

$$s_o = \frac{1}{\sqrt{1 - p^2}} = \sec\ \theta_o. \tag{2.25}$$

There is no loss of generality when applying θ_o and s_o in the co-rotating frame.

2.2 Derivation of Streamlines Near the Origin

We determine the values of θ_1, s_1, θ_2, and s_2 which represent streamlines through points close to the origin by expanding Equations 2.5 and 2.20a around θ_o and s_o respectively. For brevity, we defined parameters to simplify the expansions, $k = \theta - \theta_o$ and $t = s - s_o$, further description of these methods can be found in Appendix B (Section 5.2). The expansions result in the equations,

$$\theta_1 = \theta_o - y\ \cos(\tan\theta_o) - x\ \sin(\tan\ \theta_o), \tag{2.26a}$$

$$s_1 = s_o + [-(x s_o + y s_o\ \tan\ \theta_o)\cos(\tan\theta_o) + (y s_o - x s_o\ \tan\ \theta_o)\sin(\tan\ \theta_o)]. \tag{2.26b}$$

Using a similar method for θ_2 and s_2 we establish,

$$\theta_2 = \theta_o + y\ \cos(\tan\theta_o) + x\ \sin(\tan\ \theta_o), \tag{2.27a}$$

$$s_2 = s_o - [-(xs_o + ys_o\ \tan\ \theta_o)\cos(\tan\theta_o) + (ys_o - xs_o\ \tan\ \theta_o)\sin(\tan\ \theta_o)]. \tag{2.27b}$$

Comparing Equations 2.26 and 2.27 yields,

$$2\theta_o = \theta_1 + \theta_2, \tag{2.28a}$$

$$2s_o = s_1 + s_2, \tag{2.28b}$$

which is a useful relation representing the symmetry of the corotating frame for equal winds.

2.3 Derivation of Streamlines Far From the Origin

In this section, we find the value of θ and s, for both winds, at points far from from the stagnation point. For the first wind, we define the series,

$$\theta_f = b_0 + b_1, \tag{2.29a}$$

$$s_f = a_0 + a_1, \tag{2.29b}$$

where a and b are unknown constants, and a_1 and b_1 have an implicit p dependence. We then Taylor expand Equation 2.5 to the first order in p:

$$x_1 = 1 - s_f \cos\ \theta_f - ps_f^2 \sin\ \theta_f, \tag{2.30a}$$

$$y_1 = -\ s_f \sin\ \theta_f + ps_f^2 \cos\ \theta_f. \tag{2.30b}$$

To the zeroth order in p, ignoring the second term in Equation 2.30b and substituting in Equation 2.29, we solve for a_0 and b_0 with the result,

$$a_0 = \sqrt{(x_1 - 1)^2 + y_1^2}, \tag{2.31a}$$

$$b_0 = \arctan\left(\frac{y_1}{x_1 - 1}\right). \tag{2.31b}$$

It readily follows that to the first order in p we use the full forms of Equation 2.29 and 2.30 to solve a system of two equations for the unknowns a_1 and b_1. The expressions for a_1 and b_1 are,

$$a_1 = 0, \tag{2.32a}$$

$$b_1 = p\, a_0. \tag{2.32b}$$

The value of θ_f and s_f result from substituting Equations 2.31 and 2.32 into Equation 2.29. Expressions for θ_{2f} and s_{2f} follow from the fact that $x_2 = -x_1$ and $y_2 = -y_1$. Consequently, using the same method, we find that a_0' and a_0' are,

$$a_0' = \sqrt{(x_1 + 1)^2 + y_1^2}, \tag{2.33a}$$

$$b_0' = \arctan\left(\frac{y}{x + 1}\right). \tag{2.33b}$$

The expressions for a_1' and b_1' are identical to Equation 2.32 with the substitution of a_0' and b_0' in place of a_0 and b_0. Therefore, θ_{2f} and s_{2f} are similarly identical to Equation 2.29 with the substitution of a' and b' for the second wind.

2.4 Thin Shell Geometry

Following the approach of WS98 and WS2003, we consider a small, three-dimensional patch of shell. The normal direction can be found by taking the gradient of the function

$x - X(y)$ and evaluating for $x = X$ and finding the unit vector,

$$\hat{n}_m = \frac{\nabla[(x - X)(-1)^{m+1}]}{|\nabla(x - X)|}, \tag{2.34}$$

where subscript m allows us to choose the direction of the normal. We have defined $\hat{n}_1$ as the outward normal and $\hat{n}_2$ as the inward normal. The outward normal is therefore,

$$\begin{aligned} \hat{n}_1 = \frac{\hat{i} - \hat{j}X_y}{\sqrt{1 + X_y^2}} &= \hat{i}\ \cos\ \eta_x + \hat{j}\ \cos\ \eta_y, \\ &= \hat{i}\ \cos\ \eta_x + \hat{j}\ \sin\ \eta_x, \end{aligned} \tag{2.35}$$

where $\eta_x + \eta_y = 90^\circ$ and the subscripts on X indicate partial derivatives with respect to the subscript variable. We have defined two direction cosines and their angles relative to the x and y directions. It is important to note that for small p we require $\cos\eta_x$ to be negative and $\sin\eta_x$ to be positive. This is determined by the expected direction of the initial tilt of the collision surface deduced by the anti-parallel collision of streamlines at the stagnation point, as seen in Figure 9.From this geometry we conclude,

$$\sin\eta_x = \frac{dx/dy}{\sqrt{1 + (dx/dy)^2}}, \tag{2.36a}$$

$$\cos\eta_x = \frac{-1}{\sqrt{1 + (dx/dy)^2}}. \tag{2.36b}$$

For comparison, in the axisymmetric limit $\eta_x = \gamma$ as seen in WS98 [17]. The normal component of velocity is determined by,

$$u'_{ni} = \vec{u}'_i \cdot \hat{n}_1, \tag{2.37}$$

and the subscript i denotes either the first or second wind. The normal components of

velocity for the first wind can be written as,

$$\begin{aligned} u'_{n1} &= \cos\ \eta_x\ u_{1x} + \ \sin\ \eta_x\ u_{1y}, \\ &= \cos\ \eta_x\ [-\cos(\theta_1 - ps_1) - ps_1\ \sin(\theta_1 - ps_1) + p^2 s_1\ \cos(ps_1)] \\ &\quad + \ \sin\ \eta_x\ [-\sin(\theta_1 - ps_1) + ps_1\ \cos(\theta_1 - ps_1) - p^2 s_1\ \sin(ps_1)]. \end{aligned} \tag{2.38}$$

Using common trigonometric identities we rewrite this as,

$$u'_{n1} = -\cos(\theta_1 - ps_1 - \eta_x) - ps_1\ \sin(\theta_1 - ps_1 - \eta_x) + p^2 s_1\ \cos(ps_1 + \eta_x), \tag{2.39}$$

which for the second wind becomes,

$$u'_{n2} = \cos(\theta_2 - ps_2 - \eta_x) + ps_2\ \sin(\theta_2 - ps_2 - \eta_x) - p^2 s_2\ \cos(ps_2 + \eta_x). \tag{2.40}$$

2.5 Formulation of the Conservation Equations

In this section, we derive the full set of differential equations pertaining to the spatial components of momentum, Φ_x and Φ_y, and the conservation of mass Φ_m within the shell using the approach described by Wilkin & Stahler (2003), hereafter WS2003 [19]. We begin by considering a physical quantity Q within a three-dimensional patch, with density q, of shell. Noting that one component of the patch is the length $\Delta\ell$, we choose to represent all equations in this section as the quantity Q per unit length which allows us to consider the two dimensional geometry of the line wind in the orbital plane. In steady state, Q is constant in time. In Cartesian coordinates, the conservation law for Q may be written as,

$$\frac{\partial(Au_y q\Delta x)}{\partial y} = -\sec\ \eta_x\ [q_1 u_{n1} - q_2 u_{n2}]. \tag{2.41}$$

Note that for the case of line winds A=1. In an inertial frame, as in Section 1.2, the equations representing the spatial components of momentum could be called momentum con-

servation equations, but in a non-inertial frame or in the presence of a non-zero net force they could be referred to as force equations. Such force equations are the fluid equivalent of Newton's 2nd law, with the inclusion of the non-inertial forces. For the remainder of this paper, we may refer to the set of differential equations as conservation equations, but it should be remembered that the momentum equations are not true conservation equations in the co-rotating frame due to addition of Coriolis and centrifugal forces, which will be described below. The equation for mass is a true conservation equation regardless of reference frame. To derive the equation for mass conservation, we let Q be mass and the corresponding q be the mass density ρ. The mass conversation equation in conservative form becomes,

$$\frac{d\Phi_m}{dy} = \frac{d(\sigma_x u_y)}{dy} = -\sec\ \eta_x\ [\rho_1 u_{n1} - \rho_2 u_{n2}], \tag{2.42}$$

where $\sigma_x = \rho\Delta x$ is the mass column density in the $\hat{x}$-direction and u_y is the y-component of velocity within the shell. Similarly to W96, we define Φ_m as the mass flux within the shell [15].

In the co-rotating frame, the Coriolis and centrifugal forces are accounted for in our consideration of momentum conservation. The forces may be written as,

$$F_{\text{coriolis}} = -2\sigma_x\vec{\omega} \times \vec{u}, \tag{2.43a}$$

$$F_{\text{centrifugal}} = -\sigma_x\vec{\omega} \times (\vec{\omega} \times \vec{r}). \tag{2.43b}$$

For both spatial components of momentum, Equation 2.41 uses $q = u_i\rho$ where the subscript i denotes either the x or y-component of velocity within the shell. For the components of momentum this approach yields,

$$\frac{d\Phi_x}{dy} = \frac{d(\Phi_m u_x)}{dy} = -\sec\ \eta_x\ [\rho_1 u_{1n} u_{1x} - \rho_2 u_{2n} u_{2x}] + \sigma_x\omega^2 x + 2\sigma_x\omega u_y, \tag{2.44a}$$

$$\frac{d\Phi_y}{dy} = \frac{d(\Phi_m u_y)}{dy} = -\sec\ \eta_x\ [\rho_1 u_{1n} u_{1y} - \rho_2 u_{2n} u_{2y}] + \sigma_x\omega^2 y - 2\sigma_x\omega u_x. \tag{2.44b}$$

The Coriolis and centrifugal forces appear in component form, and vanish for no orbital motion $\omega = 0$. Equation 2.44 represents the vector momentum flux at any point in the shell. Returning to the statement of W96, the momentum within the shell is exactly the vector sum of momentum generated by both winds integrated over the shell's surface [15]. Therefore, because we know the vector momentum flux at any point we recognize that the direction of flow within the shell is parallel to the combination of Equations 2.44. Fluid in the shell follows the path of the vector momentum, and therefore moves tangential to the surface of the shell. We write a differential equation for the shape of the shell referred to as the trajectory equation,

$$\frac{dx}{dy} = \frac{\Phi_x}{\Phi_y} = \frac{u_x}{u_y}, \tag{2.45}$$

which can be used to determine the shape of the shell $x = x(y)$. The shell's shape is not a resultant of ram pressure balances between the two winds, but is determined by the direction of momentum propelled into the shell [15].

Equations 2.42, 2.44a, 2.44b, and 2.45 comprise a set of four ordinary differential equations (ODEs) in four dependent variables x, Φ_m, Φ_x, and Φ_y with independent variable y. This set of equations uses the approach of W96 in considering a trajectory equation, whereas WS98 used the normal and tangential components of momentum to determine the shape of the shell. We are able to ignore the normal and tangential component method due to the fact that the fluid in the shell follow the path of the vector sum of momentum imparted on the shell [15].

2.6 Nondimensionalization

It is convenient to convert all variables in our four differential equations into nondimensional forms. This allows the use of the nondimensional velocities taken from WH17 [18].

We define nondimensional flux functions as,

$$\tilde{\Phi}_m = \frac{\Phi_m}{\lambda}, \tag{2.46a}$$

$$\tilde{\vec{\Phi}} = \frac{\vec{\Phi}}{\lambda u_w}, \tag{2.46b}$$

$$\tilde{\Phi}_y = \frac{\Phi_y}{\lambda u_w}, \tag{2.46c}$$

$$\tilde{\Phi}_x = \frac{\Phi_x}{\lambda u_w}. \tag{2.46d}$$

The nondimensional radius is defined as $\tilde{R}_o = R_o/r_*$. We use the corresponding relations between flux functions, shown in the definitions of our four differential equations, combined with Equation 2.46 to rewrite our non-dependent variables in terms of the flux functions. The dimensionless mass column density $\tilde{\sigma}_x$ becomes,

$$\tilde{\sigma}_x = \frac{\tilde{\Phi}_m^2}{\tilde{\Phi}_y}. \tag{2.47}$$

It readily follows that the dimensionless form of Equation 2.42 is,

$$\frac{d\tilde{\Phi}_m}{dy} = -\sec\ \eta_x\ [\tilde{\rho}_1 \tilde{u}_{1n} - \tilde{\rho}_2 \tilde{u}_{2n}], \tag{2.48}$$

where $\tilde{\rho}$ is Equation 2.18. Likewise, Equations 2.44 become,

$$\frac{d\tilde{\Phi}_x}{dy} = -\sec\ \eta_x \left[\tilde{\rho}_1 u'_{1n} \tilde{u}'_{1x} - \tilde{\rho}_2 u'_{2n} \tilde{u}'_{2x}\right] + p^2 \tilde{x}' \frac{\tilde{\Phi}_m^2}{\tilde{\Phi}_y} + 2p\tilde{\Phi}_m, \tag{2.49a}$$

$$\frac{d\tilde{\Phi}_y}{dy} = -\sec\ \eta_x \left[\tilde{\rho}_1 u'_{1n} \tilde{u}'_{1y} - \tilde{\rho}_2 u'_{2n} \tilde{u}'_{2y}\right] + p^2 \tilde{y}' \frac{\tilde{\Phi}_m^2}{\tilde{\Phi}_y} - 2p\frac{\tilde{\Phi}_m \tilde{\Phi}_x}{\tilde{\Phi}_y}. \tag{2.49b}$$

Dropping the tilde notation, Equation 2.45 remains the same nondimensionally. The dimensionless set of four differential equations is now written in terms of dependent variables and known velocities which are in turn dependent on the dimensionless parameters s, θ, and p.

2.7 Singular Points and Singular Differential Equations

In this section the mathematical structure of the differential equations is discussed in terms of singular points. For a given differential equation, a singular point is defined as the point at which no analytic solution can be obtained due to the fact that there is the chance that when separating variables we divide by zero. A solution to a differential equation is called a singular solution when the solution is not unique at a specific point. In most cases there is not an analytic solution to a singular differential equation, and the solution is most probably discontinuous.

Consider the first-order autonomous differential equation with the initial condition $x(0) = 0$,

$$\frac{dx}{dt} = x^2. \tag{2.50}$$

Separating variables we find,

$$\frac{dx}{x^2} = dt. \tag{2.51}$$

Integrating the differential equation yields,

$$\frac{-1}{x} = t + C \tag{2.52}$$

and solving for $x(t)$ returns the general solution,

$$x(t) = \frac{-1}{t + C}. \tag{2.53}$$

The initial condition requires that $x(0) = 0$, but in solving for the particular solution we find that there is no value of the constant C that fits the initial condition. Therefore, $x_o = 0$ is a singular point and $x = x_o = 0$ is a singular solution to the differential equation. The singular solution must be noted in conjunction with the general solution to represent the full solution to the differential equation.

2.8 Stagnation Point Expansion

The solution to the locus of the thin shell requires integration of the set of four differential equations. However, at the stagnation point we require that the fluxes Φ_m, Φ_x, and Φ_y are identically zero. It is clear from examination of Equations 2.45, 2.48, 2.49a, and 2.49b that this produces the problem of a singular point. The singularity is produced by the vanishing denominators in those equations at the stagnation point. To escape the neighborhood of the singular point, we expand the differential equations around the stagnation point to find approximate solutions to the equations. (Note: it is the singularity that leads to the often cited condition of "normal force" or ram pressure balance at the stagnation point. Since other points along the shell are not singular points, it is inappropriate to think of ram pressure balance at locations where fluid has non-zero speed and follows a curved path.)

As mentioned previously, we expect that for $p = 0$ the thin shell is equivalent to Figure 3. We therefore develop Maclaurin series in p and y to produce approximate equations for the flux functions near the singular point. We then integrate these equations to identify the locus of the thin shell for small p. This solution acts as a check to our set of differential equations and the formalism applied to find it.

Strictly speaking, expansion in p is not required but is simpler because otherwise we would have a set of simultaneous non-linear equations which would be much more difficult to solve. Small p is also justified by physical systems of stars as the wind speed is normally higher than the orbital speed. For example, the binary system HD 931219A, shown in Table 1, has been determined to have $p \approx 0.1$ [25].

The Maclaurin expansions of Equations 2.21 and 2.25 to the second order in p results

in,

$$\theta_o = p\,(1 + \frac{1}{6}p^2), \tag{2.54a}$$

$$s_o = 1 + \frac{1}{2}p^2. \tag{2.54b}$$

We then expand θ_1, θ_2, s_1, and s_2 which enter in the velocity components u_{1x}, u_{1y}, and u_{1n}. Next, we expand the velocity components. The same steps are taken for the similar terms of the second wind. The expansion of these terms is too lengthy to write here.

At the stagnation point, located at $x = 0$, the tilt of the collision surface caused by the orbital motion of the system is specified by h_1. For $p = 0$, h_1 vanishes, but for $p > 0$ the tilt is non-zero.To derive this quantity for small p, we expand $x(y)$ to the leading order in y,

$$x = h_1\, y + h_2\, y^2 + \mathcal{O}(y^3), \tag{2.55}$$

where $h_1 = dx/dy$. The expansion of Equations 2.36, which depend on h_1, are unchanged to the lowest order. In addition, we define series for the fluxes:

$$\Phi_m = m_1\, y + m_2\, y^2 + \mathcal{O}(y^3), \tag{2.56a}$$

$$\Phi_x = f_1\, y + f_2\, y^2 + \mathcal{O}(y^3), \tag{2.56b}$$

$$\Phi_y = g_1\, y + g_2\, y^2 + \mathcal{O}(y^3). \tag{2.56c}$$

Inserting the complete set of velocity expansions into Equations 2.45, 2.48, 2.49a, and 2.49b we again expand to the second order in p and y. To the first order in y, the expansions of Equation 2.49 resemble ram pressure balance at the stagnation point. As such, both f_1 and g_1 are identically zero. The expansion of Equation 2.48 results in a non-zero m_1 which likewise implies that f_1 and g_1 vanish. To leading order in y, the outcome is a system of

four equations in four unknowns h_1, m_1, f_2, and g_2. The result is,

$$h_1 = \frac{4}{3}p + \frac{11}{6}p^3 + \frac{134}{27}p^5, \tag{2.57a}$$

$$m_1 = 2 + \frac{5}{3}p^2 + \frac{11}{3}p^4, \tag{2.57b}$$

$$f_2 = \frac{4}{3}p + \frac{11}{6}p^3 + \frac{119}{27}p^5, \tag{2.57c}$$

$$g_2 = 1 - \frac{5}{12}p^4. \tag{2.57d}$$

Examination of these equations reveals that the coefficients $h1$, m_1, f_2, and g_2 have parity in p. This important because it proves that it is not necessary to expand to higher orders in p due to the fact that the higher orders are small compared to the previous order.

2.9 Comparison with Inertial Solution

It is possible to compare Equations 2.57, which represent the initial conditions to the integration, to similar expansions of the inertial line wind collision in Section 1.2. It is necessary to set $\beta = 1$ in the inertial solution equations to have an applicable match, which means that $\theta_1 = \theta_2$. In the limit $p \to 0$ the expansions match using the following transformation, noting that the origin is shifted and there is a scale factor so that the coordinate systems match properly. The necessary transformation requires a relationship between θ_1, the independent variable in the inertial solution, and y which we find to be,

$$y = (1 - x)\,\tan\theta_1, \tag{2.58}$$

where $x = h_1 y$. But, for $p = 0$ the coefficient h_1 is also zero. This means the proper geometrical relation is,

$$y = \tan\theta_1. \tag{2.59}$$

Plugging this into Equations 2.55 and 2.56 which likewise have Equations 2.57 inserted where necessary gives us,

$$x = 0 + \mathcal{O}(\theta_1^2), \tag{2.60a}$$

$$\Phi_m = 2\big(\theta_1 + \frac{1}{3}\theta_1^3\big) + \mathcal{O}(\theta_1^6), \tag{2.60b}$$

$$\Phi_x = 0 + \mathcal{O}(\theta_1^2), \tag{2.60c}$$

$$\Phi_y = \theta_1^2 + \frac{2}{3}\theta_1^4 + \mathcal{O}(\theta_1^6), \tag{2.60d}$$

where we note that the constants h_1 and f_2 are zero for $p = 0$. Now, for comparison, we find expansions of the inertial flux functions for $\beta = 1$. For $\beta = 1$, the dimensional parameters for both winds are equivalent. The expansions of Equations 1.11, 1.12, 1.13 result in,

$$\Phi_{m,i} = 2\theta_1 + \mathcal{O}(\theta_1^6), \tag{2.61a}$$

$$\Phi_{z,i} = 0 + \mathcal{O}(\theta_1^2), \tag{2.61b}$$

$$\Phi_{y,i} = \theta_1^2 - \frac{1}{12} + \theta_1^4\mathcal{O}(\theta_1^6), \tag{2.61c}$$

$$\frac{\Phi_{z,i}}{\Phi_{y,i}} = 0 + \mathcal{O}(\theta_1^2), \tag{2.61d}$$

where we have used the subscript i to represent a nondimensionalized inertial flux function. We have defined $\Phi_{z,i}/\Phi_{y,i}$ as the trajectory equations for the inertial problem. Its result is the equivalent of h_1 in the inertial problem, and is therefore comparable to the expansion of x. In the inertial problem's coordinates, $\Phi_{z,i}$ is the equivalent of the non-inertial Φ_x. It is clear that to the leading order these expansions are in agreement.

2.10 Integration

The next step is to integrate the differential equations to determine the locus of the thin-shell. Substituting Equation 2.57 into Equations 2.55 and 2.56 produces the initial

conditions for our integration.

It is important to integrate the equations using θ and s values for points not near the origin. We use the equations derived in Section 2.3 and insert the equivalent of Equation 2.29 for both the first and second winds into every equation where θ and s are encountered in the expansions of Equations 2.45, 2.48, 2.49a, and 2.49b. Prior to this, we substitute Equation 2.55 for x_1 in Equations 2.31 and 2.33.

The set of differential equations was then integrated using the initial conditions described above for $p = 0.01$. The upper and lower bounds were $y = 0.05$ and $y = 5$. The output produces the shape of the thin-shell shown in Figure 10.

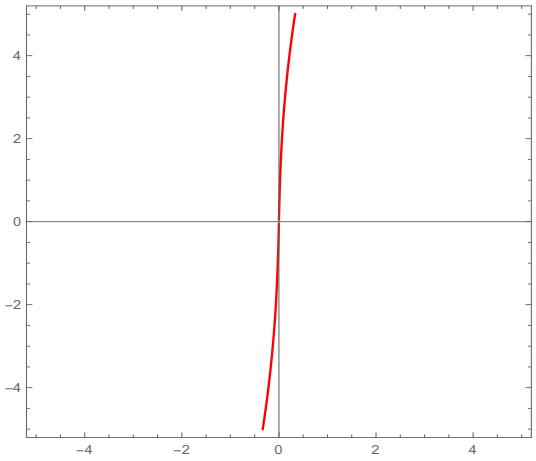

Figure 10: Shocked surface for $p = 0.01$ produced by the integration of four differential equations from $y = 0.05$ to $y = 5$.

The orbital motion twists the tail of the shock to distort the expected shell shape for no orbital motion. The shocked surface for $p = 0.01$ is comparable to the $\beta = 1$ curve shown in Figure 3 for line wind collisions with no orbital motion. Numerical integration of the differential equations yields the shell shape for small p. A family of curves is represented in Figure 11.

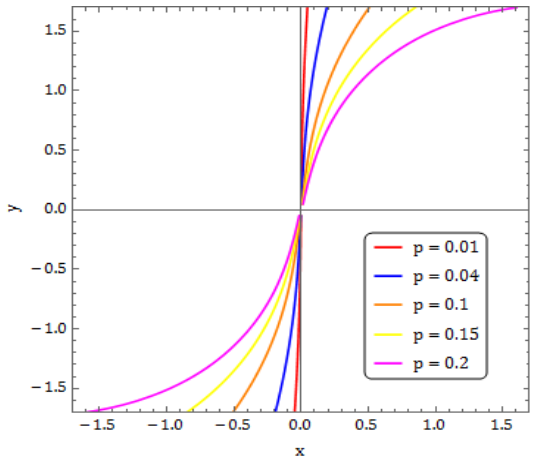

Figure 11: Numerical integration of the differential equations yields the shell shape for multiple values of p, ranging from 0.01 to 0.2.

As the orbital speed of the line-wind system increases, the effects of the Coriolis and centrifugal forces increase proportional to p and p^2 respectively. The Coriolis and centrifugal effects twist the shocked shell into a spiral structure similar to WR104 in Figure 6. The numerical integration encounters a stiff system at decreasing values of y as p increases. Therefore, we are unable to reveal the tail solution which would better represent the spiral structure of Figure 6.

3 Generalization to Unequal Winds

3.1 Nondimensionalization

We consider two line-winds with equal momentum loss rates, but unequal wind velocities or unequal mass loss rates. We define the dimensionless parameter α as a ratio of wind velocities,

$$\alpha = \frac{v_w}{v_{w2}}, \tag{3.1}$$

where v_w and v_{w2} are the velocity units of the first and second wind respectively. We continue to use Equations 2.46 and 2.47. For the first wind, the dimensionless velocity is $\tilde{u}_1 = u_1/v_w$. For the second wind, we have $\tilde{u}_2 = u_2/v_w = 1/\alpha$. It is also clear that λ and λ_2 likewise have different units. The dimensionless parameter β encapsulates λ and λ_2. The dimensionless form of Equation 2.42 with the parameters α and β is,

$$\frac{d\tilde{\Phi}_m}{dy} = -\sec\ \eta_x\ [\tilde{\rho}_1\tilde{u}_{1n} - \frac{\alpha}{\beta}\tilde{\rho}_2\tilde{u}_{2n}], \tag{3.2}$$

and Equation 2.44 becomes,

$$\frac{d\tilde{\Phi}_y}{dy} = -\sec\ \eta_x\ \left[\tilde{\rho}_1 u'_{1n}\tilde{u}'_{1y} - \frac{1}{\beta}\tilde{\rho}_2 u'_{2n}\tilde{u}'_{2y}\right] + p^2\tilde{y}'\frac{\tilde{\Phi}_m^2}{\tilde{\Phi}_y} - 2p\frac{\tilde{\Phi}_m\tilde{\Phi}_x}{\tilde{\Phi}_y}, \tag{3.3a}$$

$$\frac{d\tilde{\Phi}_x}{dy} = -\sec\ \eta_x\ \left[\tilde{\rho}_1 u'_{1n}\tilde{u}'_{1x} - \frac{1}{\beta}\tilde{\rho}_2 u'_{2n}\tilde{u}'_{2x}\right] + p^2\tilde{x}'\frac{\tilde{\Phi}_m^2}{\tilde{\Phi}_y} + 2p\tilde{\Phi}_m. \tag{3.3b}$$

Note that Equation 2.45 remains the same. The parameters α and β develop in the second wind terms only. The parameter β is set to unity for the remainder of this chapter.

3.2 Second Wind Trajectory and Velocity

In this section, we re-derive the trajectory and velocity of a fluid element emitted from the second line wind. Starting from Equation 2.19, we write this as,

$$\vec{R}_2(\tau) = -R_2(\cos(\omega\tau_2), \sin(\omega\tau_2)) - (t-\tau_2)[R_2\omega(-\sin(\omega\tau_2), \cos(\omega\tau_2)) + v_2(\cos\beta, \sin\beta)] \tag{3.4}$$

where $\beta = \pi + \theta_2 + \omega\tau_2$. We require τ_2 because for the case of unequal wind velocities fluid elements emitted from their respective winds need not be emitted at the same time to strike the same point. This is due to the fact that for α non-unity one wind has a higher velocity, and this wind requires a different, most likely shorter, s value to strike the same point as the other wind. We use the coordinate transformation from the inertial frame to the corotating frame, Equation 2.4, to get the fluid trajectory in the corotating frame. We nondimensionalize using the usual p and $s_2 = v_w(t-\tau_2)/R_o$,

$$\begin{aligned}\vec{r}_2' = \langle &- \tilde{R}_2\cos(ps_2) + \frac{s_2}{\alpha}\cos(\theta_2 - ps_2) - ps_2\tilde{R}_2\sin(ps_2), \\ &\tilde{R}_2\sin(ps_2) + \frac{s_2}{\alpha}\sin(\theta_2 - ps_2) - ps_2\tilde{R}_2\cos(ps_2)\rangle.\end{aligned} \tag{3.5}$$

The distance from the second wind to the origin is equivalent to the distance of the first wind from the origin which means that $\tilde{R}_2 = R_2/R_o = 1$. This is due to the assumption of a circular orbit. Therefore the above equation becomes,

$$\begin{aligned}\vec{r}_2' = \langle &- \cos(ps_2) + \frac{s_2}{\alpha}\cos(\theta_2 - ps_2) - ps_2\sin(ps_2), \\ &\sin(ps_2) + \frac{s_2}{\alpha}\sin(\theta_2 - ps_2) - ps_2\cos(ps_2)\rangle.\end{aligned} \tag{3.6}$$

Taking the derivative of $\vec{r}_2'$ with respect to s_2 we find the dimensionless velocity of a fluid element to be,

$$\vec{u}_2' = \langle -p^2 s_2 \cos(ps_2) + \frac{1}{\alpha}\cos(\theta_2 - ps_2) + \frac{ps_2}{\alpha}\sin(\theta_2 - ps_2), \\ p^2 s_2 \sin(ps_2) + \frac{1}{\alpha}\sin(\theta_2 - ps_2) - \frac{ps_2}{\alpha}\cos(\theta_2 - ps_2)\rangle, \tag{3.7}$$

which agrees with Equations 2.20b and 2.20c up to the appearances of α.

3.3 Second Wind Fluid Density

We re-derive the fluid density for the second line wind using the method described in Section 2.1.2. Using Equation 3.6 in conjunction with Equation 2.9 we find that the basis vectors are,

$$\mathbf{b}_{\theta 2} = \langle -\frac{s_2}{\alpha}\sin(\theta_2 - ps_2), \frac{s_2}{\alpha}\cos(\theta_2 - ps_2)\rangle, \tag{3.8}$$

and $\mathbf{b}_{s2} = \vec{u}_2'$. The magnitude square of the basis vectors are,

$$u_2'^2 = \frac{1 + p^2 s_2^2(1 + \alpha^2 p^2) - 2\alpha p^2 s_2(\cos\ \theta_2 + ps_2 \sin\ \theta_2)}{\alpha^2}, \tag{3.9a}$$

$$|\mathbf{b}_{\theta 2}|^2 = \left(\frac{s_2}{\alpha}\right)^2. \tag{3.9b}$$

We also find that $\mathrm{g}_{\theta s2} = \mathrm{g}_{s\theta 2} = \mathbf{b}_{\theta 2} \cdot \mathbf{b}_{s2} = ps^2(\alpha\, p \sin\theta - 1)/\alpha^2$. The determinant, g, of the metric tensor is,

$$\mathrm{g} = \frac{s^2(1 - \alpha\, p^2 s_2 \cos\theta_2)^2}{\alpha^4}. \tag{3.10}$$

Similarly solving Equation 2.14 using $\mathbf{A}_2 = \tilde{\rho}_2 \vec{u}_2'$ we find,

$$\sqrt{g}\tilde{\rho}_2 = f_2(\theta). \tag{3.11}$$

Matching Equation 3.11 to the behavior of the winds in the limit $s \to 0$ we find that the fluid density is,

$$\rho_2 = \frac{\lambda}{R_o u_w} \frac{\alpha^2}{s_2(1 - \alpha p^2 s_2 \cos\theta_2)}, \tag{3.12}$$

which nondimensionally is,

$$\tilde{\rho}_2 = \frac{\alpha^2}{s_2(1 - \alpha p^2 s_2 \cos\theta_2)}. \tag{3.13}$$

This is equivalent to Equation 2.18 for $\alpha = 1$, which represents the equal winds case.

3.4 Streamlines Near the Origin

Here we re-derive the equations for streamline labels representing streamlines through points close to the origin, θ_2 and s_2. As in Section 2.1.4, we use the change of variables $k_2 = \theta_2 - \theta_o$ and $t_2 = s_2 - s_o$ with the purpose of expanding in Maclaurin Series. We then use k_2 and t_2 to expand Equation 3.6. The expansion results in,

$$\theta_2 = \theta_o + \frac{\alpha[y\, p^2 s_o \alpha\ \cos(ps_o) - (ps_o x + y)\cos(ps_o - \theta_o) + x\, p^2 s_o \alpha\ \sin(ps_o) + (y\, ps_o - x)\sin(ps_o - \theta}{s_o(p^2 s_o \alpha\ \cos\ \theta_o - 1)} \tag{3.14a}$$

$$s_2 = s_o + \frac{\alpha[y\ \sin(ps_o - \theta_o) - x\ \cos(ps_o - \theta_o)]}{p^2 s_o \alpha\ \cos\ \theta_o - 1} \tag{3.14b}$$

These equations are used in the power series expansions of Equations 3.2, 3.3, and 2.45.

3.5 β Non-Unity and α Non-Unity Expansion

As for the case of equal winds, we must expand our set of four differential equations around the stagnation point to avoid a singular point. The difficulty, in the case of unequal winds (either β or α non-unity), is the possibility that the stagnation point is no longer at the origin. For β non-unity, it is well known that the stagnation point is moved closer to

the weaker wind, as seen in the inertial two wind problem. To determine the location of the stagnation point we define the arbitrary point (a, b) to be the stagnation point. The expansions for $\beta = 1$ are incredibly long, and far more complicated than when the parameter is set to unity. We were unable to complete the determination of (a, b) for β non-unity. This will be the discussion of future work.

We focused instead on $\beta = 1$ and α non-unity. The simplest way to determine whether the stagnation point is at the origin was to expand the equations about (a, b) to see if the expansions give the result $(a, b) = (0, 0)$. To do this, we set $b = 0$ and then solve for a. Expanding Equations 2.45, 3.2, 3.3a, and 3.3b in y and p we find that $a = 0$, which means that the stagnation point is in fact at the origin. This greatly simplifies the expansion, because we already know the θ and s values through the origin, and near the origin. The streamlines that strike the origin are labeled similarly by Equations 2.21 and 2.25 for both the second and first wind.

3.6 β Unity and α Non-Unity Expansion

In this section the ratio of momentum loss rates is equivalent ($\beta = 1$), therefore the stagnation point is at the origin. For the remainder of this section, the term unequal winds refers to α non-unity only. In these expansions, the equations used to represent the first wind do not change from those used in Section 2.8. The only equations that change are those for the velocity, density, and streamline labels of the second wind, which were developed in Sections 3.2, 3.3, and 3.4. We expect that the series defined for the flux functions enter at the same order as in Equations 2.55 and 2.56 where f_1 and g_1 are identically zero. This can be explained by ram pressure balance at the stagnation point, but it is simpler to consider the composition of the flux functions. The x-component of momentum flux Φ_x is defined by the series f and is a composition of Φ_m and u_x. We find that m_1, the series for the mass flux Φ_m, enters at order y, and therefore $\Phi_x = \Phi_m u_x$ must enter at a higher

order. Therefore, it makes sense that the first non-zero term in the series f and g enter at order y^2. Table 2 shows the orders of the flux function coefficients in the notation f_{ij} where i represents the order in y and j represents the order in p. It is clear that the coefficients maintain the parity of the equal winds case by alternating orders in p.

Φ_m	Φ_y	Φ_x	x
m	g	f	h
m_{10}	g_{20}	~~f_{20}~~	~~h_{10}~~
~~m_{11}~~	~~g_{21}~~	f_{21}	h_{11}
m_{12}	g_{22}	~~f_{22}~~	~~h_{12}~~
~~m_{13}~~	~~g_{23}~~	f_{23}	h_{13}
m_{14}	g_{24}	~~f_{24}~~	~~h_{14}~~
~~m_{15}~~	~~g_{25}~~	f_{25}	h_{15}

Table 2: The coefficients for the flux function series are shown. The notation, using f as an example, f_{ij} shows the order of y and p respectively. The slashes indicate coefficients that have been verified to vanish, demonstrating the given functions have either even or odd parity to this order.

To the leading order, we find that the coefficients h_1, m_1, f_2, and g_2 are,

$$h_1 = \frac{2(2+\alpha+\alpha^2)}{3(1+\alpha)}p + \frac{4(2+\alpha+\alpha^2)^2(3+\alpha+2\alpha^2)}{27(1+\alpha)^3}p^3, \tag{3.15a}$$

$$m_1 = 1+\alpha^2+\frac{2(1+\alpha^2)(2+\alpha+\alpha^2)}{3(1+\alpha)}p^2, \tag{3.15b}$$

$$f_2 = \frac{1}{3}(2+\alpha+\alpha^2)p + \frac{(2+\alpha+\alpha^2)(21+\alpha(16+\alpha(31+2\alpha(3+5\alpha))))}{27(1+\alpha)^2}p^3, \tag{3.15c}$$

$$g_2 = \frac{1}{2}(1+\alpha)+\frac{3+2\alpha+5\alpha^2+2\alpha^4}{6(1+\alpha)}p^2. \tag{3.15d}$$

These represent the first two non-zero terms in orders of p. In our integrations we use the first three non-zero terms, but they are too long to write here. The first order terms match our previous work, Equation 2.57, for the case of equal winds, $\alpha = 1$.

3.7 Integration

Substituting Equation 3.15 into Equations 2.55 and 2.56 determines the initial conditions for the integration of our set of differential equations. The determination of θ and s values, in Section 2.8, for points far from the stagnation point remains the same in the case of unequal winds. This is the case for both the first and second wind.

Numerical integration of the four differential equations, using the initial conditions in Equation 3.15 returns the shell shape. The output produces the shape of the thin shell shown in Figure 12. The upper and lower bounds were $y = 0.05$ to 6 with $p = 0.1$ and $\alpha = 0.1$.

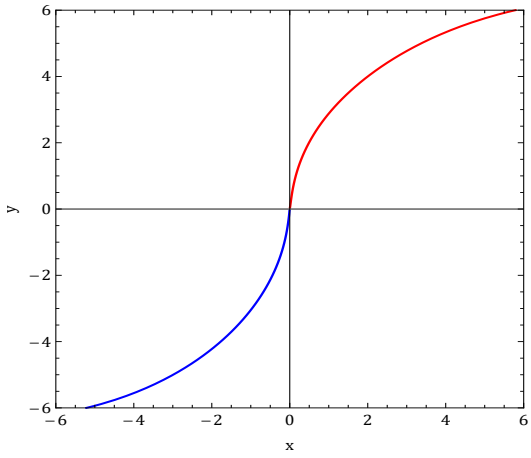

Figure 12: Unequal winds shell for $p = 0.1$ and $\alpha = 0.1$ integrated from $y_i = 0.05$ to $y_f = 6$. A different color is used for the top and bottom halves of the shell to demonstrate that the breaking of symmetry in the α non-unity case.

For the case of unequal winds, which for $\alpha = 0.1$ is equivalent to the second wind having a ten times faster wind velocity, it is expected that the axisymmetry of the shell is broken. To demonstrate the breaking of symmetry, we plot both halves of the shell shown in Figure 12 in the same quadrant; this is done in Figure 13.

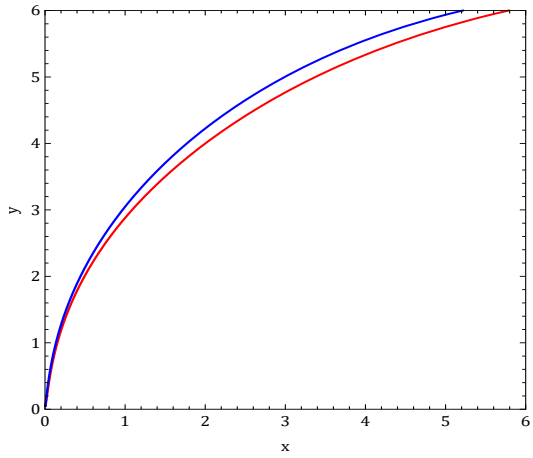

Figure 13: Both halves of the shell shown in Figure 12 have been plotted in the same quadrant to demonstrate the broken symmetry of the problem.

Figure 13 clearly represents the broken symmetry of the α non-unity case. The curves are no longer perfectly overlayed, and do not follow the same curve as they did in the equal winds case for $\alpha = 1$. Near the stagnation point, the Coriolis term dominates and is the leading cause of asymmetry. This is due to the scaling of the Coriolis term which is $\propto pv$. In the wind with a lower velocity, the Coriolis term is less significant. On the other hand, the centrifugal term, which scales as $\propto p^2 y$, increases with distance and therefore far from the stagnation point this term becomes more dominant. In Figure 14, we show the full curves for $\alpha = 0.1, 0.5, 1$ similarly with $p = 0.1$.

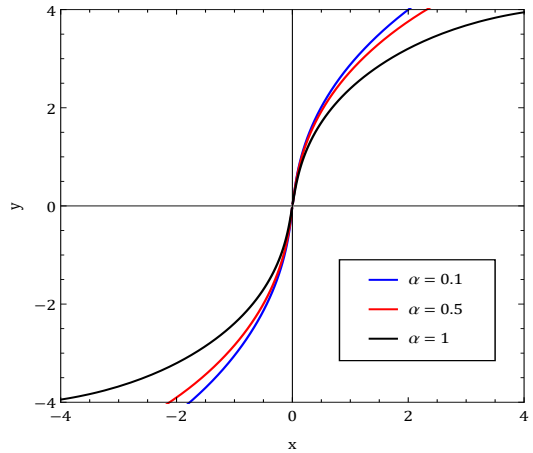

Figure 14: Different Shell shapes for $p = 0.1$ with $\alpha = 0.1$ in blue, $\alpha = 0.5$ in red, and $\alpha = 1$ in black. Note that $\beta = 1$.

Figure 14 shows that as the velocity of the second wind increases, the solutions become more distorted from the equal winds shell. This represents the importance of the parameter α in fully describing the possible shell structures for binary line wind collisions. Table 1 also presses the significance of α, the stellar binaries shown in the table are all of unequal wind speeds. It is therefore critical to study α as a parameter to allow for meaningful comparisons with physical systems.

3.8 Tilt of the Collision Surface

The tilt of the collision surface is an important factor to grasp prior to beginning an integration of these differential equations. The expansions return the tilt of the collision surface as $h_1 = dx/dy$ which is given by Equation 3.15a. It is important to note that the tilt of the collision surface is not a necessary factor for non-rotating systems like the one described in Section 1.2. The tilt is pivotal to the full description of the physics of this problem, and beginning the integration at the correct angle with respect to the symmetry axis is important in correctly representing the structure of the collision surface. Parkin et al. found a skew angle μ which is the angle relative to the symmetry axis of the collision surface and the line of centers of the stars [29],

$$\tan\ \mu = \frac{v_{orb}}{v_w} = p, \tag{3.16}$$

where we have determined that $\tan\ \mu$ is equivalent to the definition of our parameter p. It is also worth noting that Lamberts et al. uses the skew angle in their simulations of colliding wind binaries [24]. Lamberts et al. notes that μ remains small for systems where orbital motion is unimportant, which is in agreement with our determination of its proportionality to our parameter p. We compare the tilt given by the skew angle with our h_1. To convert μ

to a slope, where it is simple to plot it alongside h_1, we use simple trigonometry to find,

$$m = \cot\ \mu = \frac{1}{p}, \tag{3.17}$$

where m is the slope associated with the skew angle. A comparison of the slope given by Equation 3.15a versus the slope m is shown in Figure 15.

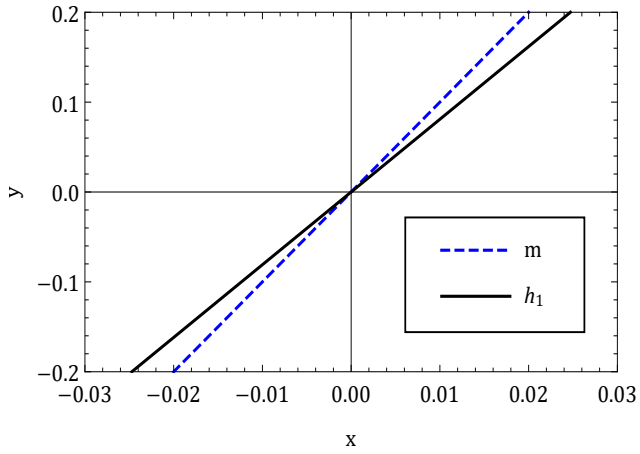

Figure 15: A comparison between the tilt given by Parkin et al. m and the tilt found through the Taylor expansion method h_1.

There is a significant difference between the two slopes. Numerically we find that h_1 is approximately 80% of m.

4 Conclusions

Binary star collisions are a well observed phenomenon in astrophysics. The winds emitted from both stars collide to form a shocked structure, which due to the orbital motion of the system is distorted into a spiral pattern. Hydrodynamic simulations have been successful in predicting the shape of these structures [29] [24], but simple analytic models have yet to be found when both Coriolis and centrifugal forces are accounted for. In this paper, we formulated a method for finding the shocked structure shape using analytic methods and numerical integration techniques.

We demonstrated the concept of a line wind to serve as a simplification to a difficult problem. A line wind emits fluid radially away from a line and has a density $\rho \propto 1/r$ (cylindrical radius) whereas a point wind's density scales $\propto 1/r^2$ (spherical radius). We applied the CRW96 flux function consideration of mass and momentum to the line wind geometry to solve for the shape of the unmoving two line wind collision surface. A flux function describes the rate of flow of a property, in this case mass, linear, and angular momentum, through an area. Flux function descriptions allow for simple conservation of mass and momentum arguments within the shell that give the shape of the curve. We demonstrated that the line wind analogy to the analytic solution of CRW96 has a simpler form, and most notably does not require numerical solutions for the value of θ_2. For winds with equal momentum loss rates, we find that the shell produced in the unmoving two wind interaction (Figure 3) is commensurate with the shell for no orbital motion in a binary line wind system. This line wind analogy serves as a useful introduction to the concept of a line wind, as well as a possible comparison for future work. It is also possible to provide simpler forms for W96's analytic solution for stellar wind bow shocks.

We have presented the formalism applicable to the binary line wind system with orbital motion. We considered the line winds in the corotating frame, the reference frame of

the line winds, and therefore included Coriolis and centrifugal effects. The symmetry of the corotating frame allowed us to consider steady state solutions which meant that the necessary differential equations are ordinary differential equations (ODEs). We derived a set of four ODEs representing the momentum and conservation of mass in the shell. The line wind geometry removes one dependent variable Φ_z and one independent variable z, which makes the problem more tractable. The trajectory and velocity of fluid elements in the corotating frame is borrowed from WH17, where we altered their formulas to fit the line wind geometry and determined the trajectory and velocity for a second wind. The wind density also follows from the method described by WH17. Taylor expansion of the differential equations was necessary to avoid a singular point at the origin. The singular point is caused by the vanishing coefficient multiplying a higher order derivative at this location. This is caused by the fact that the velocity of fluid in the shell starts at zero at the origin which means that the mass and linear momentum fluxes at the origin are zero. Following successful Taylor expansions, we find the necessary initial conditions that allow for numerical integration of the four ODEs. We first solved the orbiting line wind collision problem for equal winds with both β and α unity, where β is a ratio of wind momenta and α is a ratio of wind speeds. For small values of the dimensionless parameter p, which represents the line winds orbital speed versus the wind launch speed, the shocked surface (Figure 10) is similar to the CRW96 analogy shell (Figure 3).

Furthermore, we followed the same formalism for the equal winds case and applied it to systems where the stellar wind speeds are not equivalent, α non-unity. It is clear from Table 1 that in many binary systems the wind velocities of the primary and secondary stars are not equivalent. This provides context for the decision to consider the α non-unity case. This case required a new non-dimensionalization of the differential equations, wind velocities and trajectories, and the wind density due to the fact that the unit of wind speed is no longer the same for both winds. As in the equal winds case, the stagnation point is located at the origin and we were forced to Taylor expand the equations to avoid the singular point.

We determined that there is a clear asymmetry in the shells produced in this case. This is caused by the Coriolis and centrifugal terms at different length scales from the stagnation point. Further work is required to allow for β non-unity and unequal mass stars. These cases move the stagnation point and the center of mass which creates a difficult problem.

We derived analytic equations representing a streamline through a specific value along the x-axis. We also demonstrate that our Maclaurin series methods using k and t are accurate to first order and do not necessarily require higher order corrections. This is important due to the fact that higher order coefficients become difficult to handle. Proving that approximate functions to the first order are acceptable was helpful in completing the Taylor expansions of the differential equations for both the equal winds case and α non-unity.

The results of the binary line wind interaction can not be directly compared to observations of binary star systems, because stars do not have cylindrical symmetry. The relevance of this work is to develop a method for solving binary wind collisions with orbital motion that will be applicable to stars with isotropic winds, removing the line wind approximation. This requires a substantially more complicated geometrical model. This work serves as an important stepping stone, and reaffirms the usefulness of analytic work in the theory of stellar winds. Future work will be done to remove the simplification of line winds and solve the isotropic wind collision problem with orbital motion.

5 Appendix

5.1 Appendix A: Streamlines

The flow of fluid elements radially from each line wind are described by streamlines, an example is shown in Figure 16.

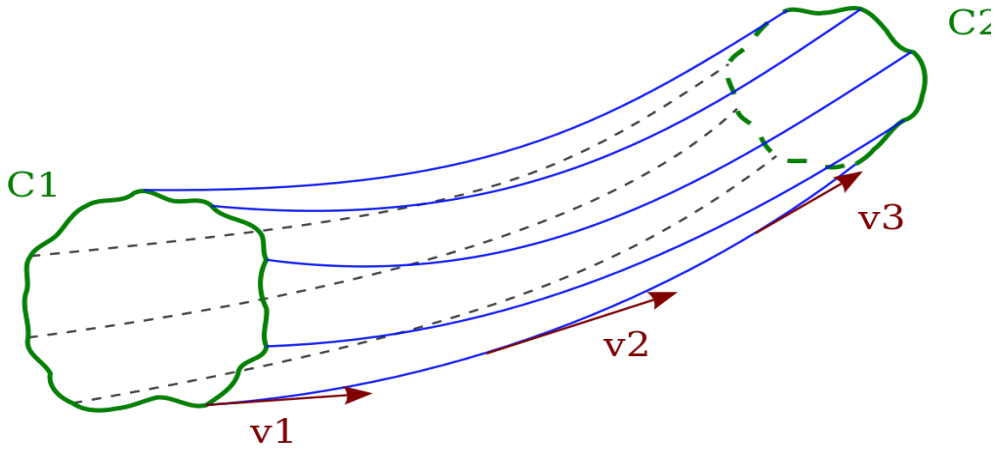

Figure 16: A streamtube bounded by streamlines. The arrows represent the velocity tangential to the streamlines. Taken from Wikipedia.

It is important to note, that streamlines cannot cross one another because it is physically impossible for a fluid to have two different velocities at the same point in space at a given time. Fluid may not cross the streamlines by the same physical reasoning; the streamlines describe the flow of the fluid and they therefore move in the same direction.

Streamlines are described mathematically by a stream function (ψ). The stream function describes the path of a fluid element that is always tangent to the velocity, $\vec{u}$, in the same way that electric field lines are always tangent to $\vec{E}$ [21]. To understand how the stream function is defined we must first consider the divergence of the flow ($\nabla \cdot F$). In fluid mechanics, the physical definition of the divergence of a vector field is the rate at which density dissipates through a given region. With respect to the streamtube represented in Figure 16, the continuity equation of fluid mechanics states that the rate at which density

changes inside the streamtube is proportional to the mass flux of the fluid flowing out of the streamtube,

$$\nabla \cdot (\rho \vec{u}) = -\frac{\partial \rho}{\partial t} \tag{5.1}$$

where $\vec{u}$ is the flow velocity vector of the fluid. Often, stream functions are defined for incompressible fluids, this assumes that the density of the fluid is uniform and constant and therefore obeys the approximation that $\nabla \cdot (\vec{u}) = 0$. In the case of the line-wind, we have a compressible fluid due to the fact that the density of the line-wind changes with distance ($\propto \frac{1}{r}$) from z-axis. Therefore, in the steady state approximation, and to conserve mass flux through the stream tube $\nabla \cdot (\rho \vec{u}) = 0$ must be satisfied by the stream function. This states that the rate of mass $\rho A u$, where A is the surface area of the opening, through one end of the streamtube is the same as the mass flux through the opposite end. Consequentially, $\rho A u = constant$.

However, we must now examine a two-dimensional velocity field parallel to the xy-plane that is tangential at every point to the flow of fluid along the shell. In cartesian coordinates the continuity equation therefore becomes,

$$\frac{\partial(\rho u_1)}{\partial x} + \frac{\partial(\rho u_2)}{\partial y} = 0 \tag{5.2}$$

where u_1 and u_2 are the respective velocity components of $\vec{u}$. We can introduce a vector stream function Ψ that describes the flow velocity for an incompressible flow as,

$$\vec{u} = \nabla \times \vec{\psi} \tag{5.3}$$

where $\psi = (0, 0, \psi)$ is normal to the flow velocity vector $\vec{u} = (u_1, u_2, 0)$. Note that when the flow velocity is described in the form of Equation 5.3 the continuity equation is automatically satisfied by $\nabla \cdot (\nabla \times A) = 0$ [21]. For a compressible flow in steady state,

we define a vector function $\vec{f} = \rho\vec{u}$ which we substitute into Equation 5.3 in place of $\vec{u}$,

$$\vec{f} = \nabla \times \vec{\psi} \tag{5.4}$$

and as a result of Equation 5.4,

$$\vec{f} = \frac{\partial\psi}{\partial y}\hat{i} - \frac{\partial\psi}{\partial x}\hat{j} \tag{5.5}$$

and replacing $\vec{f} = \rho\vec{u}$ we find that the flow velocity vector equals,

$$\vec{u} = \frac{1}{\rho}\frac{\partial\psi}{\partial y}\hat{i} - \frac{1}{\rho}\frac{\partial\psi}{\partial x}\hat{j} \tag{5.6}$$

therefore the components of the flow velocity vector are,

$$u_1 = \frac{1}{\rho}\frac{\partial\psi}{\partial y} \quad \text{and} \quad \mathrm{u_2} = -\frac{1}{\rho}\frac{\partial\psi}{\partial \mathrm{x}} \tag{5.7}$$

providing the solution to Equation 5.2. In cylindrical coordinates the velocity vector components become,

$$u_r = \frac{1}{\rho r}\frac{\partial\psi}{\partial\theta} \quad \text{and} \quad \mathrm{u_\theta} = -\frac{1}{\rho}\frac{\partial\psi}{\partial \mathrm{r}} \tag{5.8}$$

where r is the cylindrical radius. Now, consider two points in the two-dimensional plane $P = (x, y)$ and $Q = (x + dx, y + dy)$, where dx and dy are infinitesimal distances of separation. It is clear that,

$$\begin{aligned}\psi(x + dx, y + dy) - \psi(x, y) &= \frac{\partial\psi}{\partial x}dx + \frac{\partial\psi}{\partial y}dy \\ &= \nabla\psi \cdot d\vec{r}\end{aligned} \tag{5.9}$$

if ψ has the same value at both points P and Q then the two points lie on the same streamline. The equation of the streamline is therefore $\psi = c$, where c is a constant. As shown in Figure 16, lines of constant stream function are streamlines. It is clear that $d\vec{r}$ is tangent to

the streamline $\psi = c$ at P and Q. It follows from Equation 5.9 that,

$$\nabla\psi \cdot d\vec{r} = 0 \tag{5.10}$$

which implies that $\nabla\psi$ is normal to the streamline from P to Q. Because the streamfunction is everywhere tangent to the flow velocity vector in the shell $\vec{u} \cdot \nabla\psi = 0$. It is important to note that a change in the value of the stream function is equal to the mass flow rate between the two streamlines,

$$\Phi_m = \int_1^2 d\psi = \psi_1 - \psi_2 \tag{5.11}$$

where Φ_m is the mass flow rate per unit length, for the case of the line-wind. It is important to recognize that throughout this thesis the angles θ_1 and θ_2 are specific streamlines and are therefore equivalent to ψ_1 and ψ_2 in this appendix. It is possible to write a similar analytic equation for Φ_m for the binary line wind collision problem in terms of θ_1 and θ_2. The an analytic solution for Φ_m can be understood by inspection of Figure 9. The amount of mass flowing along the shell does not depend on where the streamlines strike the shell, but instead is determined by the number of streamline striking the shell between specific θ values for the two winds. Due to the plane geometry, all the mass flux striking the shell between given streamlines must flow along the shell to conserve mass. The analytic solution is,

$$\Phi_m = \lambda_2 (\theta_2 - \theta_o) - \lambda_1 (\theta_1 - \theta_o). \tag{5.12}$$

The analytic solution requires information about the shape of the shell, thus we used the differential equation for Φ_m (Equation 2.48) in our numerical integration, and subsequently used the analytic solution as a check on the numerical integration for Φ_m. The solution depends only on the streamline launch angles as θ_o is a constant for a specific value of p. For winds with both β and α set to unity the mass flux simplifies to $\Phi_m = \theta_2 - \theta_1$.

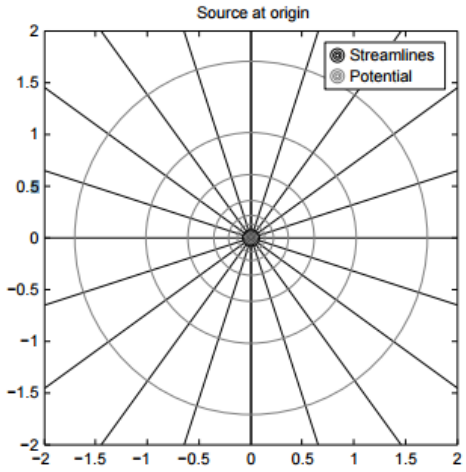

Figure 17: The radial lines extending from the source at the origin are streamlines, and the circles surrounding the origin are lines of constant velocity potential. [23]

5.2 Appendix B: Streamline Description

In this appendix, we discuss the computation of the streamline equations as well as techniques for manipulating the equations. The streamline equations for a line wind located at $x = 1$ is Equation 2.5, and is represented visually in Figure 9. There is a clear importance to streamlines through the origin in the equal wind case, $\alpha = 1$, as it represents the streamlines that collide at the stagnation point. But, it is equally important to have a description of streamlines that intersect with the x-axis.

Using the FindRoot function in Mathematica, we solved Equation 2.5 for the streamline labels, θ and s, that represent streamlines passing through the points $(x, 0)$, where x is from 0 to 1. We did this for five p values ranging from 0.01 to 0.9 to show the progression of θ and s values required to strike the x-axis as the rotation of the system increases. The results are represented in Figure 18.

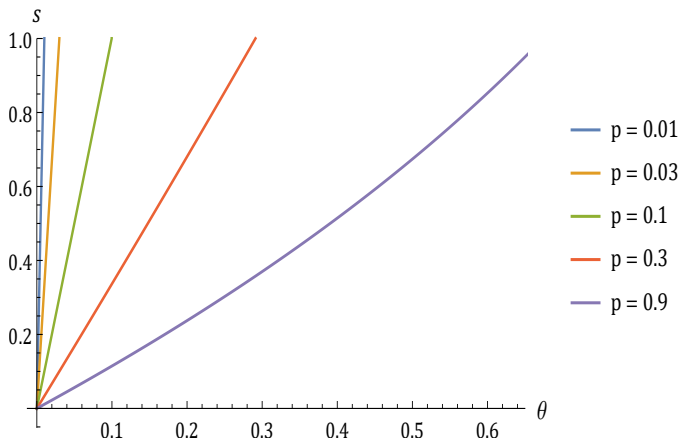

Figure 18: Plot of s versus θ for the point on a given streamline that lies on the x-axis for values of p from 0.01 to 0.9.

As p increases, the parameter s also increases for a streamline through a specific x-value. This is due to the rotation of the system, and the greater angle the streamline must rotate before striking the x-value. In Figure 19, we plot a geometric representation of the numerical calculations presented in Figure 18. This figure visually represents the streamlines represented by the values plotted in Figure 18 for $p = 0.9$.

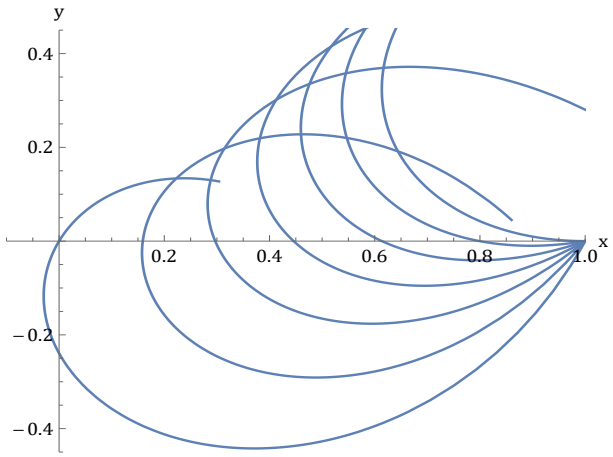

Figure 19: Streamlines that intersect the x-axis for $p = 0.9$ plotted for θ values from 0 to θ_o in steps of $\theta_o/6$.

From Figure 19, we can clearly visualize the useful information in Figure 18. It is clear that as θ increases the s value required to strike the x-axis increases as well. We expect to observe the same action for smaller values of p, but there would be less visual streamline

crossings this close to the x-axis and substantially less curvature of the streamlines. The cusp region, described by WH17, moves further from the origin. The cusp is defined as the innermost point on the shock surface, for a more in depth description see WH17 [18]. The streamline that initially enters the cusp tangentially has θ and s values given by,

$$\theta_{cusp} = \theta_o, \tag{5.13a}$$

$$s_{cusp} = \frac{1}{p^2\sqrt{1-p^2}}. \tag{5.13b}$$

The streamline that enters the cusp tangentially is the same streamline that passes through the origin. It is also clear that s_{cusp} has a similar form to s_o with an extra factor of p^2 in the denominator.

In Figure 20, we plot the θ values for streamlines crossing $(x, 0)$ versus the x values where the streamline intersects the x-axis. Note that the intersection of the plotted lines with $x = 0$ are θ values of streamlines through the origin. These values agree with the analytic solution for a streamline through the origin found by Equations 2.21 and 2.25.

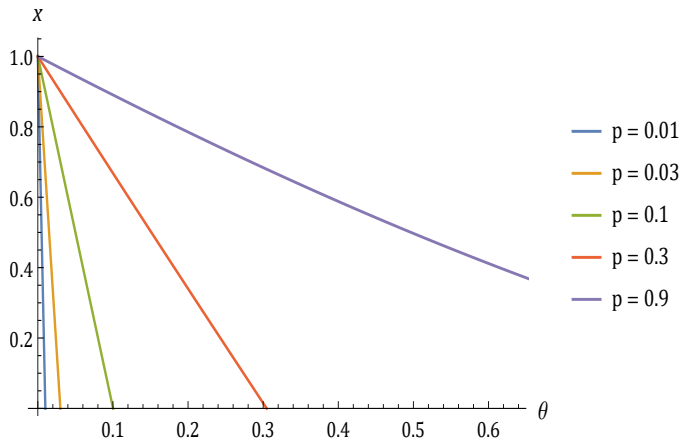

Figure 20: Plot of x versus θ for values of p from 0.01 to 0.9.

In Figure 20, we observe that as p increases the value of θ also increases which fits with the prior observation from Figure 18 showing a similar increase in s. Both of these changes in streamline label values through specific x-values are caused by the increased rotation of

the system for larger p values. Also, as $x \to 1$, we require the streamline initially tangent to the x-axis, which is labeled by $\theta = 0$. Therefore, it is expected that all of the plotted lines originate similarly from $(x, \theta) = (1, 0)$.

We use the analytic solution for the θ value of the streamline that strikes the origin, θ_o, in conjunction with the fact that the lines plotted in Figures 18 and 20 appear largely linear to develop an analytic fit to the numerical root solutions. The analytic fit to the data represented in Figure 18 is,

$$s_{analytic} = (1 - x)\, s_o, \tag{5.14}$$

where s_o is given by Equation 2.25. This linear interpolation is indeterminate for $p \geq 1$ due to the inclusion of s_o. Likewise, the analytic fit to Figure 20 is,

$$\theta_{analytic} = (1 - x)\, \theta_o, \tag{5.15}$$

where θ_o is represented mathematically by Equation 2.21. From Equations 5.14 and 5.15, it is easy to see that both of the analytic fits have similar forms. We performed a test to check the accuracy of our analytic fits by comparing the values provided by the analytic fit to the numerical roots. To do this, we subtract the value determined by the numerical solution from the value given by the analytic fit for a specific value of x. The differences between the values are plotted in Figure 21. We do not divide by the value of the analytic fit because it causes an asymmetry to appear in the residual plots.This is due to the fact that for different x-values we divide by numbers ranging three orders of magnitude.

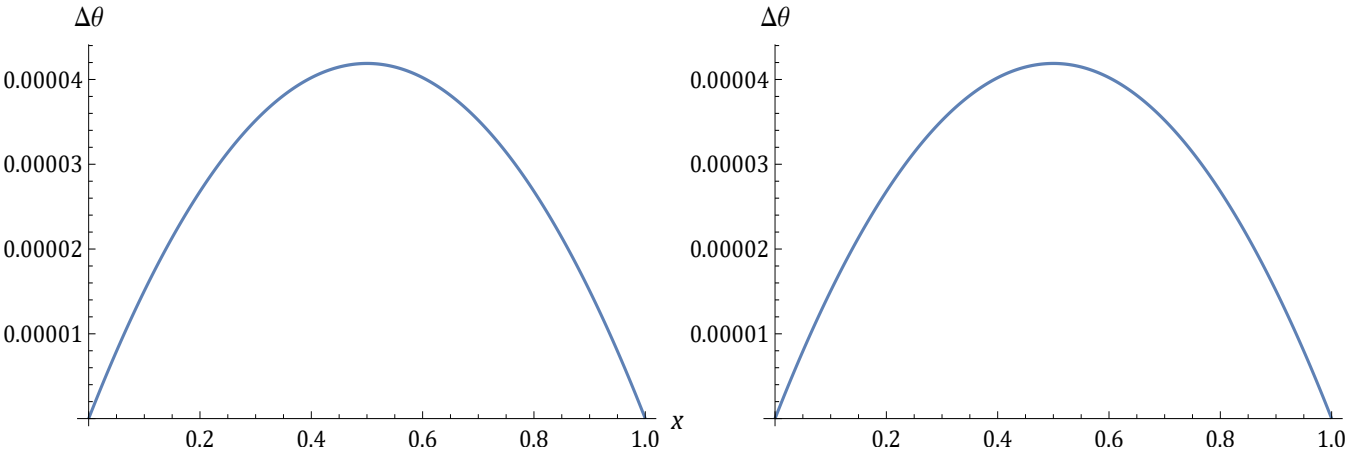

Figure 21: Residual plots representing the difference between the numerical solution and analytic solution for θ and s-values, given by Equations 5.14 and 5.15, through the points $(x, 0)$.

Figure 21 proves that the analytic fit is accurate to five decimal places. Therefore, the analytic fit is a good approximation for streamline labels through $(x, 0)$.

5.3 Appendix C: Expansion of θ and s

The determination of certain θ and s values that constitute streamlines through specific points given by (x, y) is important, most generally for the case of stagnation points. But, of equivalent importance are equations for streamlines that pass through points a small distance away from the stagnation point. Such equations are necessary to Taylor expand the conservation equations about the stagnation point. As discussed briefly in Section 2.1, Equations 2.26 and 2.27 were determined by expanding Equations 2.5 and 2.20a around θ_o and s_o. In this section, we elaborate on the technique used to handle this expansion.

In Wolfram Mathematica, the command Series is used to Taylor expand a given expression. The order and variable of expansion are specified through the Series command. As stated, the goal of our expansion of Equations 2.5 and 2.20a was to find θ and s values that produce streamlines through arbitrary points close to the stagnation point. Recognizing that the streamline through the stagnation point was given by θ_o and s_o we naturally

expanded about those values. But, to develop Maclaurin series, which are much simpler, we developed the change of variables to k and t where,

$$k = \theta - \theta_o, \tag{5.16a}$$

$$t = s - s_o. \tag{5.16b}$$

These equations allow us to expand the streamline equations to develop a series in k and t to the first-order. The expansions develop series of the form,

$$x = x_{10}\, k + x_{01}\, t + x_{11}\, kt, \tag{5.17a}$$

$$y = y_{10}\, k + y_{01}\, t + y_{11}\, kt, \tag{5.17b}$$

where the x and y coefficients are determined by the series, and are strictly functions of p. In the above equations, there is a kt cross term that seemingly should not develop to the first-order in k and t. But, consider the possibility that a large change in k is matched by a small change in the parameter t, or vice versa. In this case, the magnitude of the cross term may be similar to the normal first-order k and t terms, and therefore should be kept. To check the magnitude of the cross term we solved Equation 5.17a for k and t keeping the cross term, and then again without the cross term. When using the cross term, we find quadratic solutions to k and t, and when ignoring the cross term we develop linear solutions. To test the size of the cross term correction we define the function f to represent the relative size of the cross term correction to the linear solutions that ignore the cross term,

$$f = \sqrt{\left(\frac{t_{cross} - t_{linear}}{t_{linear}}\right)^2 + \left(\frac{k_{cross} - k_{linear}}{k_{linear}}\right)^2}, \tag{5.18}$$

where the t and k terms are functions of x, y, and p. This function, f, is plotted in Figure 22 for the range $-0.1 \leq x \leq 0.1$ and $-0.3 \leq y \leq 0.3$ for $p = 0.1$.

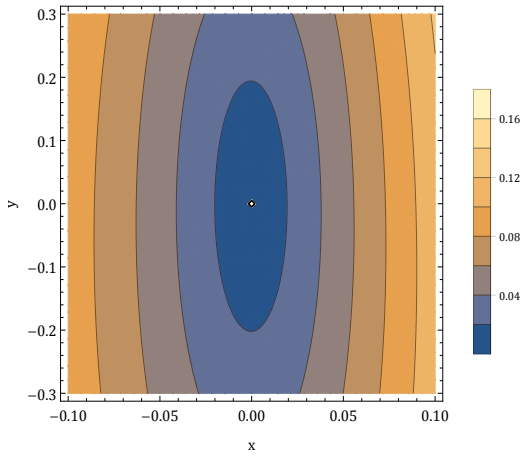

Figure 22: Contour plot representing Equation 5.18 for the range $-0.1 \leq x \leq 0.1$ and $-0.3 \leq y \leq 0.3$ for $p = 0.1$.

From Figure 5.18, we see that as expected the contour plot depends more on one variable than the other, in this case it depends more on x than y. A large change in y is required to match a small change in x, which means that it may be required to keep the cross term for certain values of x and y. However, from the contour plot we can visualize that for small values of x and y that represent points near the origin, the cross term correction may not be necessary.

References

[1] Paul Murdin, "Encyclopedia of Astronomy and Astrophysics," Nature Publishing Group (2001).

[2] John C. Brandt, "Introduction to the Solar Wind," W. H. Freeman and Company (1970).

[3] "A close halo of large transparent grains around extreme red giant stars," Nature 484 (2012): 220-222.

[4] "X-ray emission from interacting wind massive binaries: a review of 15 years of progress," Advances in Space Research 58 (2016), 761-781.

[5] M. F. Corcoran, X-Ray Emission From Colliding Wind Binaries, in: V. Niemela, N. Morrell, P. Pismis, S. Torres-Peimbert (Eds.), Revista Mexicana de Astronomia y Astrofisica Conference Series, volume 5 of Revista Mexicana de Astronomia y Astrofisica Conference Series, 1996, pp. 54–60.

[6] "Colliding Winds in Low-Mass Binary Star Systems: wind interactions and implications for habitable planets," Astronomy & Astrophysics 577 (2015), A122.

[7] C.R. Kitchin, "Optical Astronomical Spectroscopy," Institute of Physics Publishing (1995).

[8] Robert C. Smith, "Observational Astrophysics," Cambridge University Press (1995).

[9] Jean-Paul Koninx, "Aspects of Stellar Wind Theory," (1992).

[10] "Observing stellar wind bow shocks," arXiv: 1005.1527 (2010).

[11] "Double Bow Shocks Around Young, Runaway Red Supergiants: Application to Betelgeuse," The Astrophysical Journal 751 (2012).

[12] Dave Van Buren, "Stellar Wind Bow Shocks," ASP Conference Series, Vol. 35, 1993.

[13] "A dusty pinwheel nebula around the massive star WR 104," Nature 398 (1998): 487-489.

[14] "The Prototype Colliding-Wind Pinwheel WR 104." The Astrophysical Journal 675.1 (2008): 698-710.

[15] "Exact Analytic Solutions for Stellar Wind Bow Shocks." The Astrophysical Journal 459 (1996): L31-L34.

[16] "Exact Algebraic Solutions of the Thin-shell Two-wind Interaction Problem." The Astrophysical Journal 469 (1996): 729-735.

[17] "The Condfinement and Breakout of Protestellar Winds: Quasi-steady solution," The Astrophysical Journal 502 (1998): 661-675.

[18] Wilkin & Hausner (2017), Astrophysical Journal (Submitted).

[19] "Trapped Protostellar Winds and Their Breakout." The Astrophysical Journal 590 (2003): 917-931

[20] "Modeling Nonaxisymmetric Bow Shocks: Solution Method and Exact Analytic Solutions." The Astrophysical Journal 532 (2000): 400-414.

[21] David J. Griffiths, "Introduction to Electrodynamics," Fourth Edition, Pearson Education, Inc. (2013).

[22] Jerry B. Marion, "Classical Dynamics of Particles and Systems," Academic Press (1965).

[23] Houghton et al., "Aerodynamics for Engineering Students," Elsevier Ltd. (2013).

[24] "Impact of orbital motion on the structure and stability of adiabatic shocks in colliding wind binaries," Astronomy & Astrophysics 546 (2012).

[25] del Palacio, S., Romero, G. E., Bosch-Ramon, V., & Benaglia, P. 2016, Boletin de la Asociacion Argentina de Astronomia La Plata Argentina, 58, 225

[26] Gosset, E., & Nazé, Y. 2016, Astronomy & Astrophysics, 590, A113

[27] Bloecker, T. 1995, Astronomy & Astrophysics, 297, 727

[28] Wilkin, F. P., Canto, J., & Raga, A. C. 1997, Herbig-Haro Flows and the Birth of Stars, 182, 343

[29] "A 3D dynamical model of the colliding winds in binary systems," arXiv: 0805.4529 (2008).

[30] Leitherer, C., Robert, C., & Drissen, L. 1992, The Astrophysical Journal, 401, 596.

[31] Lemaster, M. N., Stone, J. M., & Gardiner, T. A. 2007, The Astrophysical Journal, 662, 582

[32] De Becker, M., Rauw, G., Pittard, J. M., et al. 2004, Astronomy & Astrophysics, 416, 221

[33] Dyson, J. E., Hartquist, T. W., & Biro, S. 1993, Mon. Not. R. Astron. Soc., 261, 430

[34] Girard, T., & Willson, L. A. 1987, Astronomy & Astrophysics, 183, 247

[35] Luo, D., McCray, R., & Mac Low, M.-M. 1990, The Astrophysical Journal, 362, 267

[36] Lamberts, A., Fromang, S., & Dubus, G. 2011, Mon. Not. R. Astron. Soc., 418, 2618

[37] Zhekov, S. A., and Skinner, S. L. (2015) X-rays from the oxygen-type Wolf-Rayet binary WR30a, Mon. Not. R. Astron. Soc. 452, 872–877.

[38] Parkin, E. R., and Gosset, E. (2011) Investigating the X-ray emission from the massive WR+O binary WR 22 using 3D hydrodynamical models, Astronomy & Astrophysics 530, A119.